JGR Solid Earth

RESEARCH ARTICLE
10.1029/2025JB033223

Density of Sodium Aluminosilicate Melts Along the $NaAlSiO_4$-$NaAlSi_3O_8$ Join at High Pressure: In-Situ Measurements and Re-Calibration of a Modified Hard-Sphere Equation of State For Silicate Melts

Man Xu[1,2,3], Zhicheng Jing[4], James A. Van Orman[5], Qingyang Hu[1], Qi Chen[3], Tony Yu[3], and Yanbin Wang[3]

[1]Center for High Pressure Science and Technology Advanced Research, Shanghai, China, [2]Shanghai Advanced Research in Physical Sciences, Shanghai, China, [3]Center for Advanced Radiation Sources, The University of Chicago, Chicago, IL, USA, [4]Department of Earth and Space Sciences, Southern University of Science and Technology, Shenzhen, China, [5]Department of Earth, Environmental, and Planetary Sciences, Case Western Reserve University, Cleveland, OH, USA

Abstract Silicate melts play a crucial role in planetary differentiation. The density contrast between silicate melts and the surrounding solid residue exerts a primary control on many magmatic processes. However, direct measurements of the density of silicate melts at high pressure (P) and temperature (T) conditions remain challenging, particularly for the highly viscous and reactive silica- and alkali-rich melts. Here we determined the high P-T densities of three sodium aluminosilicate melts with nepheline ($NaAlSiO_4$), jadeite ($NaAlSi_2O_6$), and albite ($NaAlSi_3O_8$) compositions, using the high-P X-ray microtomography technique up to 4.1 GPa and 2020 K. Our results suggest that the substitution of $(NaAl)^{4+}$ for Si^{4+} along the $NaAlSiO_4$-$NaAlSi_3O_8$ join leads to higher melt density and lower melt compressibility. In addition, our new data, combined with a wide range of literature data, were employed to re-calibrate a modified hard-sphere equation of state (HS-EOS) for silicate melts, which provides a unified framework for calculating the density and other compressional properties of multi-component silicate melts in the CaO-MgO-Al_2O_3-SiO_2-FeO-Na_2O-K_2O (CMASFNK) system up to ~25 GPa. The calibration also reveals that SiO_2, alkalis, and CaO are the major components contributing to the compositional dependence of melt elastic properties. The HS-EOS was then applied to alkali basaltic melts at cratonic mantle conditions and silica- and alkali-rich melts at early planetesimal melting conditions, with implications for the gravitational stability and extraction of melts in Earth's mantle and planetesimal settings.

Plain Language Summary Density of silicate melts is crucial for our understanding of magmatic processes inside Earth and terrestrial planets. However, the density of silicate melts at high pressure (P) and temperature (T) conditions, corresponding to those in planetary interiors, is still not well-constrained, particularly for those highly viscous and reactive silica- and alkali-rich melts. In this study, we focus on sodium aluminosilicate melts along the $NaAlSiO_4$-$NaAlSi_3O_8$ join and determined their densities up to 4.1 GPa and 2020 K using the high-P microtomography technique. Our new data, combined with a large set of literature data, were used to re-calibrate a modified hard-sphere equation of state (HS-EOS) for silicate melts. This model, incorporating the effect of P, T and composition, can serve as a unified framework for calculating the density of silicate melts in the CaO-MgO-Al_2O_3-SiO_2-FeO-Na_2O-K_2O system. Applying our HS-EOS to alkali basaltic melts at cratonic mantle conditions shows that these melts are buoyant and will tend to migrate upwards to interact with the cratonic roots. Evaluating the buoyancy overpressure generated by silica- and alkali-rich melts in early planetesimals using our HS-EOS suggests that dyke formation due to buoyancy overpressure is unlikely to be the major mechanism for efficiently extracting melts in planetesimals.

Key Points:

- Density of sodium aluminosilicate melts were measured at high pressure and temperature using in situ microtomography technique
- The substitution of $(NaAl)^{4+}$ for Si^{4+} along the $NaAlSiO_4$-$NaAlSi_3O_8$ join leads to higher melt density and lower melt compressibility
- A universal hard-sphere equation of state was calibrated for silicate melts with implications for melt stability and extraction

Supporting Information:

Supporting Information may be found in the online version of this article.

Correspondence to:

M. Xu and Z. Jing,
man.xu@hpstar.ac.cn;
jingzc@sustech.edu.cn

Citation:

Xu, M., Jing, Z., Van Orman, J. A., Hu, Q., Chen, Q., Yu, T., & Wang, Y. (2026). Density of sodium aluminosilicate melts along the $NaAlSiO_4$-$NaAlSi_3O_8$ join at high pressure: In-situ measurements and re-calibration of a modified hard-sphere equation of state for silicate melts. *Journal of Geophysical Research: Solid Earth*, *131*, e2025JB033223. https://doi.org/10.1029/2025JB033223

Received 18 OCT 2025
Accepted 18 JAN 2026

Author Contributions:

Conceptualization: Man Xu, Zhicheng Jing
Data curation: Man Xu
Formal analysis: Man Xu
Funding acquisition: Man Xu, Zhicheng Jing, Qingyang Hu, Yanbin Wang
Investigation: Man Xu, Zhicheng Jing, Qi Chen, Tony Yu
Methodology: Man Xu, Zhicheng Jing, Tony Yu, Yanbin Wang
Project administration: Man Xu, Zhicheng Jing

1. Introduction

Silicate melts are ubiquitous in Earth and other terrestrial planets and play an important role in their chemical evolution and dynamics. As the major carrier of heat and incompatible elements, they are largely responsible for the formation of crusts and mantle heterogeneities observed geochemically and geophysically (Blundy & Dalton, 2000; Nakagawa & Tackley, 2012; Shankland et al., 1981). The density contrast between silicate melts and the surrounding mineral phases exerts a primary control on many igneous and magmatic processes. For example, accurate knowledge of melt density is required to model the near-surface segregation and migration of

Resources: James A. Van Orman, Qingyang Hu, Tony Yu, Yanbin Wang
Software: Man Xu, Zhicheng Jing
Supervision: Zhicheng Jing, James A. Van Orman, Yanbin Wang
Validation: Man Xu
Visualization: Man Xu
Writing – original draft: Man Xu
Writing – review & editing: Man Xu, Zhicheng Jing, James A. Van Orman, Qingyang Hu, Qi Chen, Yanbin Wang

buoyant magmas (Faul, 2001) and to understand the dynamics of volcanic eruptions (Malfait, Seifert, Petitgirard, Perrillat, et al., 2014). The occurrence of neutrally or negatively buoyant melts in planetary interiors, on the other hand, would have significant implications for the geochemical evolution and geophysical anomalies deep inside the planets (Agee, 1998; Sanloup, 2016; Stolper et al., 1981). In addition, many terrestrial planets are believed to have had at least one magma ocean stage in their early history (Elardo et al., 2011; Elkins-Tanton et al., 2003). The thermodynamic modeling of magma ocean solidification processes also requires knowledge of the high-pressure density of silicate melts. Thus, the equation of state for silicate melts with a wide range of compositions is fundamental to understanding the evolution of our Earth and other terrestrial planets.

Despite its importance, the density and equation of state of silicate melts at high pressures are still not well-constrained due to difficulties in direct experimental measurements on melts at high pressure and temperature conditions. In addition, natural magmas comprise a potentially infinite, multi-dimensional continuum of compositions (Thomas & Asimow, 2013), thus requiring the development of a reliable tool to model melt density based on limited experimental data. Although the density of silicate melts has been determined for a wide range of compositions, from peridotitic (Sakamaki et al., 2010), basaltic (Agee, 1998; Ohtani & Maeda, 2001), granitic (Malfait, Seifert, Petitgirard, Perrillat, et al., 2014), to hydrous ultramafic melts (Jing & Karato, 2012; Matsukage et al., 2005) by a variety of techniques, the EOS obtained in these studies are mostly empirical and can only be applied to calculate the density of the specific melt compositions studied. Thus, this approach of determining EOS individually is far from sufficient for the wide composition range of silicate melts relevant to planetary differentiation. Another approach is to determine the density of selected end-member compositions (e.g., diopside, anorthite) and intermediate compositions (e.g., model basalt) and use these to calibrate a mixing model for the molar volume as a function of melt composition. The density of any melt composition in between can then be calculated. The mixing model (mostly linear) approach has been demonstrated successfully for silicate melts by several pioneering works at room-pressure conditions (Bottinga et al., 1982; Kress & Carmichael, 1991; Lange & Carmichael, 1987; Rivers & Carmichael, 1987), enabling the calculations of density and compressibility of silicate melts at 1-atm for a wide range of compositions and temperatures. Extension of such mixing models to high pressure either utilizes certain expansion of volume in terms of pressure such as the Taylor expansion (e.g., Lange, 1994) and the Pade expansion (Ghiorso, 2004), or the Birch-Murnaghan equation of state (e.g., Jing & Karato, 2008, 2009). But all these empirical approaches have difficulties in calibrating the compositional dependences of higher-order expansion parameters with limited experimental data due to the lack of a physical model.

To extend the EOS of multi-component silicate melts to higher pressures, a modified hard-sphere EOS was proposed by Jing and Karato (2011), which can well explain the compressional behaviors of silicate melts and provides a unified EOS formulism for multi-component silicate melts. However, the modified hard-sphere EOS has only been calibrated to the CMASFH (CaO-MgO-Al_2O_3-SiO_2-FeO-H_2O) system (Jing & Karato, 2011, 2012). The effect of the Na_2O component has yet been constrained at high pressures, despite its importance in low-degree melt generation in Earth's deep mantle (Takazawa et al., 1998) and in early planetesimals (Collinet & Grove, 2020). This is partly due to the difficulty in measuring the density of Na_2O-rich melts at high pressures with the most commonly used techniques for melt density measurements such as the sink-float (e.g., Agee, 1998; Agee & Walker, 1993; Ghosh et al., 2007; Jing & Karato, 2012; Knoche & Luth, 1996; Matsukage et al., 2005) and X-ray absorption techniques (Malfait, Seifert, Petitgirard, Perrillat, et al., 2014; Sakamaki et al., 2010; Seifert et al., 2013), because Na_2O-rich melts often have high viscosity, high reactivity, and low X-ray absorption. In addition, the Na_2O component in silicate melts may not always follow linear mixing behavior (Ghiorso & Kress, 2004; Jing & Karato, 2011; Kress et al., 1988), possibly due to the interaction between the Na_2O and Al_2O_3 components to maintain local charge balance. Thus, more density data on Na_2O-bearing melts are needed at high pressures to extend the hard-sphere EOS (HS-EOS) model to a broader range of silicate melts.

Here we determined the high-pressure density of three Na_2O-rich melts along the $NaAlSiO_4$-$NaAlSi_3O_8$ join using our newly developed high-pressure X-ray microtomography technique for silicate melts (Xu, Jing, Van Orman et al., 2020). Our new data provide an improved basis for constraining the effect of Na_2O on the compressional properties of silicate melts. Combined with a large set of literature data, the modified hard-sphere EOS model was re-calibrated for multi-component silicate melts in the CMASFNK (CaO-MgO-Al_2O_3-SiO_2-FeO-Na_2O-K_2O) system. Analyses using this HS-EOS allowed a better understanding of the stability of low-degree alkali-rich melts in planetary interiors with implications for melt extraction processes in Earth's mantle and planetesimal settings.

Table 1
Composition of Recovered Samples (Mol%)

	SiO_2	Al_2O_3	Na_2O
Ab	75.9 (0.9)	13.2 (0.1)	10.9 (1.0)
Jd	65.8 (0.5)	17.7 (0.2)	16.5 (0.7)
Ne	50.5 (0.3)	26.5 (0.2)	23.0 (0.4)

Note. The compositions were measured by EDS and recalculated as oxides. Numbers in parentheses represent one-standard deviation of multiple measurements.

2. Materials and Methods

2.1. Starting Materials

The starting materials were prepared by mixing reagent-grade chemical powders of Na_2CO_3, Al_2O_3 and SiO_2 (Alfa Aesar, 99.99% purity) in appropriate ratios in an agate mortar under ethanol for ~2 hr. The mixture was then dried and decarbonated using a platinum crucible at 1173 K in a high-temperature box furnace for ~24 hr. The full release of CO_2 in the mixture was confirmed by checking the mixture weight before and after decarbonation. The decarbonated mixture was then fused at 1873 K for ~4 hr and quenched to a glass by removing the crucible rapidly from the furnace and immersing the crucible bottom in water. The fusion process was repeated twice to ensure the homogeneity of the obtained glass. Sodium loss during the fusion is insignificant as demonstrated by the measured compositions of the recovered samples from the experiments (Table 1). The resulting bubble-free, transparent glass was then machined to a cylindrical disk with 1.6 mm outer diameter and 1.0 mm thickness using a CNC-milling machine. The machined glass disks were used as the starting samples for high-pressure experiments. Before each experiment, the weight of the glass disk was measured using a Scientech SM50 high-precision analytical balance at GSECARS with a resolution of 0.01 mg. The measured weights were 5.242 ± 0.029 mg for the albite (Ab) glass, 3.080 ± 0.018 mg for the jadeite (Jd) glass (smaller sample size than normal due to chip of the glass during machining), and 5.319 ± 0.027 mg for the nepheline (Ne) glass. The weights were averaged from at least 5 repeated measurements for each sample.

2.2. High-Pressure X-Ray Microtomographic Experiments

Volumetric measurements of liquid samples were enabled by in situ X-ray microtomographic experiments at high pressures and temperatures. The detailed experimental procedures have been described in Xu, Jing, Van Orman, et al. (2020) and therefore are only briefly summarized here. To produce a 3D volume rendering of the sample, the entire cell assembly containing the sample needs to be rotated by 180° with radiographs taken at each 0.5° angular increment. This was achieved using a 250-ton press equipped with a tomography module at GSECARS Beamline 13-BM-D of the Advanced Photon Source (APS), enabling rotation of the cell under load up to 50 tons (Wang et al., 2005; Yu et al., 2016). A modified Paris-Edinburgh (PE) cell was used for high-pressure generation (Figure 1). The pressure medium is X-ray transparent boron epoxy. The heater, thermal insulator, and electrodes are made of graphite, zirconia, and tantalum, respectively. Molybdenum was used to encapsulate the sample under high *P-T* conditions because it has relatively low reactivity and strong X-ray absorption contrast with silicate melts (Xu et al., 2018; Xu, Jing, Van Orman et al., 2020). A pink beam was used for the tomographic scans, which enables faster data collection than using a monochromatic beam (Rivers, 2016) and greatly reduces the time that the samples stay at high temperatures. The experimental pressure was determined from the energy-dispersive X-ray diffraction of the MgO pressure standard in the cell assembly using the EOS of MgO (Tange et al., 2009), and temperature was estimated using power-temperature curves calibrated in separate experiments using exactly the same cell assembly (Xu, Jing, Van Orman et al., 2020). The uncertainties are within ±0.5 GPa for pressure, and within ±100 K for temperature.

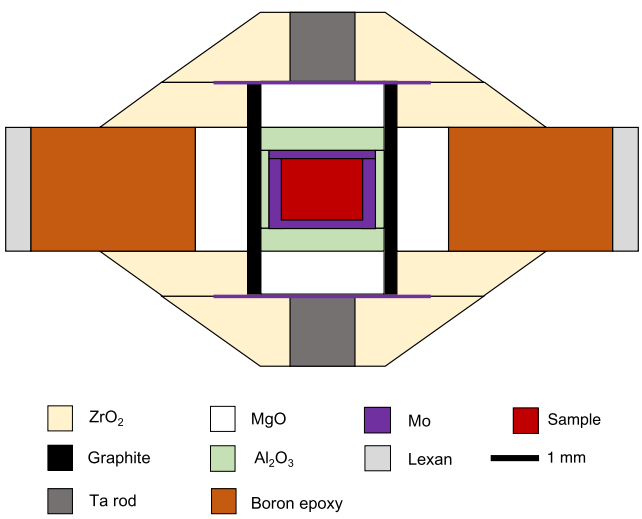

Figure 1. Drawing of the PE cell assembly designed for density measurements on silicate melts using the high-pressure microtomography technique.

For each experiment, the pressure was first increased to the target load, after which the sample temperature was raised above its liquidus curve (Figure 2). Three compression-heating cycles were performed for each experiment, with maximum achieved pressure of 4.1 GPa and temperature of 2020 K, respectively. The experiments were quenched by turning off the heater power. The recovered samples were analyzed using an SEM at GSECARS and the Center for Nanoscale Materials of Argonne National Laboratory. The recovered samples were transparent, homogenous glasses, confirming the complete melting of the samples during the experiments (Figure 2). No leakage of the melt sample from the capsule was observed in the quenched

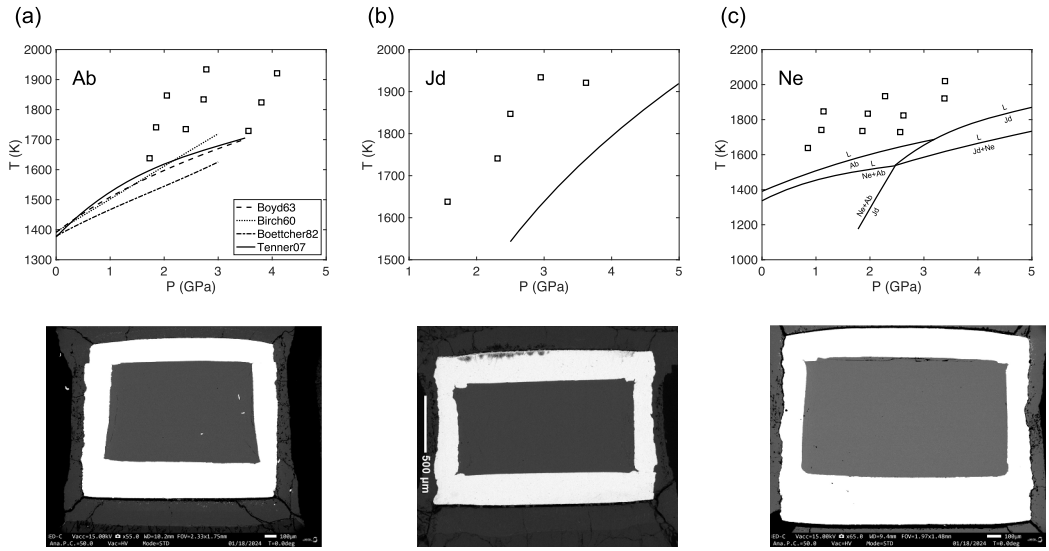

Figure 2. Experimental *P-T* conditions, melting curves, and SEM images of the recovered products for (a) Ab melt, (b) Jd melt, and (c) Ne melt. Melting curves for Ab are from several studies including Boyd et al. (1963), A. F. Birch and LeComte (1960), Boettcher et al. (1982), and Tenner et al. (2007). The melting curve for Jd is from Litvin and Gasparik (1993), and the melting phase relations for Ne are from Bell and Roseboom (1969). All experimental P-T conditions were above the corresponding liquidus temperatures for each phase, and the recovered samples were all homogeneous glasses.

products. The measured compositions of the recovered samples were close to the ideal stoichiometric compositions and no significant molybdenum contamination was detected (Table 1).

2.3. Data Analysis

Tomographic reconstruction involves: (a) subtracting background dark current and flat field intensities from the raw radiographic images; (b) correcting rotation center and minimizing ring artifacts; and (c) performing the Radon transform and grid reconstruction to produce 2D slices perpendicular to the rotation axis. All these steps were accomplished using the IDL program Tomo_Display at GSECARS (Rivers & Wang, 2006), which uses the high-speed Gridrec FFT algorithm and can reconstruct the slices in parallel on multiple CPU threads. Figure 3a shows one reconstructed horizontal slice (viewed from the top) of the Jd melt sample at 3.6 GPa and 1921 K. The sample can be clearly distinguished from the molybdenum capsule. The reconstructed horizontal slices were imported into ImageJ and Blob3D (Ketcham, 2005) for additional filtering and sample segmentation (Figure 3b). The pixel size (1.687 μm for both horizontal and vertical direction) and slice distance (1 pixel) form an effective voxel size of 4.801 μm^3. A mean filter was applied to the imported slices to smooth out noisy pixels and enhance the contrast between the sample and Mo capsule (Lesher et al., 2009; Xu, Jing, Van Orman et al., 2020). The voxel intensity ranges of the sample and capsule were carefully examined in Blob3D, and the sample volume was then

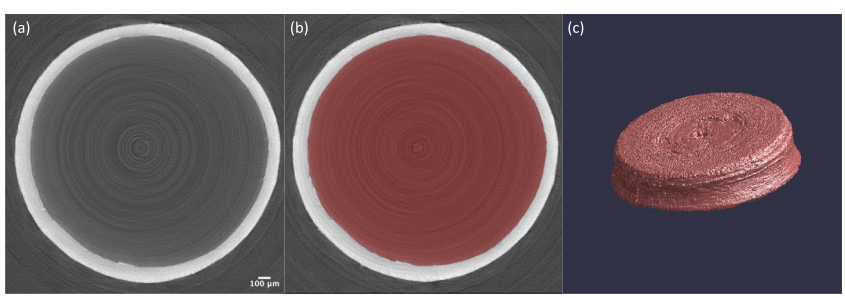

Figure 3. (a) A reconstructed slice from the *Z* direction (viewing from the top) of the Jd melt sample at 3.6 GPa and 1,921 K. (b) Segmentation of the sample from surrounding molybdenum capsule using advanced thresholding methods in Blob3d. (c) Reconstructed 3D volume rendering of the sample.

Table 2
Experimental Conditions and Results

Composition	Load (tons)	P (GPa)	T (K)	V (mm^3)	ρ (g/cm^3)
Ab	10	1.73	1,638	2.095	2.502
	10	1.85	1,741	2.077	2.524
	10	2.05	1,847	2.109	2.486
	20	2.40	1,735	2.032	2.580
	20	2.73	1,834	2.022	2.592
	20	2.78	1,934	2.046	2.562
	30	3.56	1,729	1.991	2.633
	30	3.80	1,824	1.943	2.698
	30	4.09	1,921	1.961	2.673
Jd	10	1.57	1,638	1.225	2.514
	10	2.31	1,741	1.210	2.546
	20	2.50	1,847	1.182	2.606
	20	2.95	1,934	1.187	2.595
	30	3.62	1,921	1.159	2.658
Ne	10	0.85	1,638	2.142	2.483
	10	1.10	1,741	2.155	2.468
	10	1.14	1,847	2.154	2.469
	20	1.86	1,735	2.095	2.539
	20	1.96	1,834	2.105	2.527
	20	2.28	1,934	2.096	2.538
	30	2.56	1,729	2.030	2.620
	30	2.62	1,824	2.022	2.630
	30	3.38	1,921	2.022	2.630
	30	3.39	2,020	2.048	2.597

Note. The uncertainty is less than ±0.5 GPa for pressure and less than ±100 K for temperature. The total uncertainty in determined densities is within 1.2%.

segmented from the capsule using various thresholding methods available in BloB3D (Ketcham & Carlson, 2001; Xu, Jing, Van Orman et al., 2020).

After segmentation, the sample can be easily separated from the surrounding voxel volumes, and its total volume was obtained from the summation of the voxel volumes occupied by the sample (Figure 3c). The sample volume (~1 mm^3) is more than eight orders of magnitude larger than the voxel size (4.801×10^{-9} mm^3), providing a high resolution for 3D volume measurements. The uncertainty in the measured volumes mainly comes from the thresholding process, and is estimated to be ~1% based on the deviations of reconstructed volumes (~0.015 mm^3) obtained by adjusting the threshold value slightly. The density was then obtained by dividing the mass of the glass sample measured before each experiment by the reconstructed sample volume. The total uncertainty in the obtained density can be estimated by propagating errors from mass (~0.6%) and volume measurements (~1.0%) as $\sigma_\rho \approx \sqrt{\sigma_M^2 + \sigma_V^2} = 1.2\%$.

3. Results

3.1. High-Pressure Densities of Sodium Aluminosilicate Melts

The experimental conditions and results are reported in Table 2. Measured densities are plotted as functions of pressure in Figure 4, after correcting to the 1,773 K isotherm using the thermal expansion coefficients calculated for each melt from the temperature dependences of the partial molar volumes of the oxide components (Lange, 1997). The room-P densities were also calculated from the linear mixing model using the partial molar volumes of oxides (Lange, 1997). The obtained high-P densities for albite (Ab), jadeite (Jd) and nepheline (Ne) melts increase monotonically with pressure, with Ne melt having the highest density and Ab melt having the lowest density, respectively, in the investigated experimental pressure range. For Ab melt, our measured densities are higher than those predicted from the fusion curve analysis of albite (Tenner et al., 2007). As the high-P density obtained from fusion curve analysis strongly depends on the accuracy of the position of the melting curve as well as a range of thermodynamic parameters for both the solid and melt phase, it could have large uncertainties if there are any inconsistencies in the melting curve (e.g., Figure 2a) or poorly constrained parameters during the calculation. For Jd melt, our new results are significantly lower than those from our previous study using the same experimental approach (Xu, Jing, Van Orman et al., 2020) and higher than those obtained in Sakamaki (2017) using X-ray absorption method (Figure 4b). A re-examination of the quenched sample from our previous study shows that a small portion of the melt sample may have leaked out of the capsule during the experiment, resulting in smaller apparent sample volume, hence an overestimate on density and compressibility (Figure S1 in Supporting Information S1). The present experiments do not have any leakages as evidenced from the SEM analysis on recovered samples (Figure 2). The density obtained from Sakamaki (2017) may have suffered from some background correction issues due to the low X-ray absorption contrast between the sodium-rich melt and surrounding cell assembly materials. The derived bulk modulus K_{T0} (19.0 GPa) for Jd melt in our current study show excellent consistency with the value (19.6 GPa) derived from the room-pressure ultrasonic measurements on Na_2O-Al_2O_3-SiO_2 melt system (Kress et al., 1988). For comparison, previous study by Xu, Jing, Van Orman, et al. (2020) reported a much smaller value of K_{T0} (10.8 GPa) due to the potential sample leakage as noted in SI Figure S1 in Supporting Information S1, and the study by Sakamaki (2017) reported a somewhat higher value (21.5 GPa). Thus, the current data set can be considered to be more accurate than previous density measurements. For Ne melt, to our best knowledge, there are no other available density data to compare with our measurements.

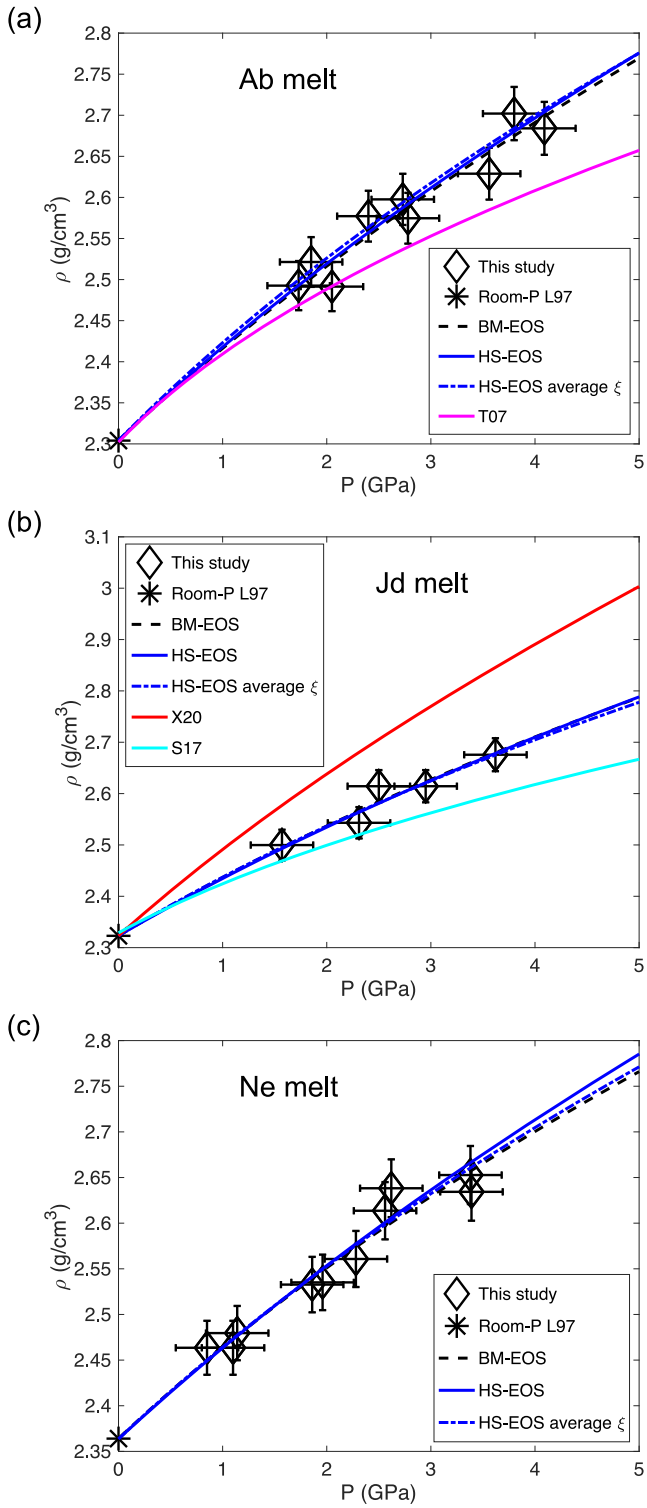

Figure 4. Experimental and fitting results for (a) Ab melt, (b) Jd melt, and (c) Ne melt. The room-P density for each melt is calculated from the linear mixing model L97 (Lange, 1997). BM-EOS: Birch-Murnaghan equation of state, HS-EOS: hard-sphere equation of state (Jing & Karato, 2011), hard-sphere equation of state (HS-EOS) average ξ: HS-EOS with an average of the deformability of spheres (ξ), see detailed discussion in Section 3.3. T07-Tenner et al. (2007), X20-Xu, Jing, Van Orman, et al. (2020), S17-Sakamaki (2017).

3.2. Data Fitting Using the Birch-Murnaghan EOS

The Birch-Murnaghan EOS (BM-EOS) was derived from the finite strain theory for solids (F. Birch, 1947) and has also been widely used to fit the density data for geological melts at high pressures (e.g., Agee, 1998; Sakamaki et al., 2010; Sanloup et al., 2013; Seifert et al., 2013). Here we first fit our data using the third-order BM-EOS, which relates pressure (P) and high-P density (ρ) as follows:

$$P = \frac{3K_{T0}}{2}\left[\left(\frac{\rho}{\rho_0}\right)^{\frac{7}{3}} - \left(\frac{\rho}{\rho_0}\right)^{\frac{5}{3}}\right]\left\{1 + \frac{3}{4}\left(K'_{T0} - 4\right)\left[\left(\frac{\rho}{\rho_0}\right)^{\frac{2}{3}} - 1\right]\right\}. \quad (1)$$

The BM-EOS has three parameters, the room-P density (ρ_0), the room-P bulk modulus (K_{T0}), and the pressure derivative of bulk modulus at room P (K'_{T0}). All three parameters are temperature and composition dependent. For ρ_0 and K_{T0}, they can be calculated using the linear mixing model as a function of partial molar quantities at a reference temperature as:

$$\rho_0 = \frac{\sum_i M_i X_i}{\sum_i \overline{V}_{0i} X_i}, \quad (2)$$

$$K_{T0} = -\frac{\sum_i \overline{V}_{0i} X_i}{\sum_i \frac{\partial \overline{V}_i}{\partial P} X_i}, \quad (3)$$

where X_i, M_i, $\overline{V}_{0i}$, and $\frac{\partial \overline{V}_i}{\partial P}$ are the molar fraction, molar mass, partial molar volume and its pressure dependence of the i-th oxide component in the melt. For the fitting, we first fixed ρ_0 for each melt to the values calculated from the calibrated partial molar volumes and their temperature dependences by Lange (1997). All our high P-T density data were corrected to the 1773 K reference isotherm using $\rho = \rho_{T\mathrm{ref}} \exp[-\alpha(T)(T - T_{\mathrm{ref}})]$, where $\alpha(T)$ is the thermal expansion coefficient for silicate melts, also obtained from the liner mixing model by Lange (1997). Here it was assumed that the effect of pressure on $\alpha(T)$ is small up to ~4 GPa. A Monte-Carlo approach was then used to fit the density data and to estimate the uncertainties in the fitting parameters (Xu et al., 2018; Xu, Jing, Bajgain, et al., 2020). The best-fit values for K_{T0} and K'_{T0} were found by minimizing χ^2, defined as

$$\chi^2 = \sum_i \frac{\left(\rho_i^{\mathrm{data}} - \rho_i^{\mathrm{model}}\right)^2}{\left(\sigma_i^{\rho}\right)^2}, \quad (4)$$

where ρ_i^{data} is the high-P density data, ρ_i^{model} is the modeled density from BM-EOS using randomly generated values of K_{T0} and K'_{T0}, and σ_i^{ρ} is the uncertainty in measured density including both the uncertainty from density measurements and the propagated equivalent uncertainty in density due to the uncertainty in pressure. We explored the parameter range 5–25 GPa for K_{T0} and 3–13 for K'_{T0}. The fitting results are shown in Table 3. Due to the trade-offs between K_{T0} and K'_{T0} (Bass et al., 1981), the fitting results have large uncertainties, almost covering the entire range for the parameter spaces set for the fitting. This basically means that density data in a limited pressure range is unable to uniquely constrain both K_{T0} and K'_{T0} for the BM-EOS. Therefore, we also fixed the K_{T0} based on the linear mixing model for Na_2O-Al_2O_3-SiO_2 melts calibrated by the room-P ultrasonic measurements (Kress et al., 1988) to fit only the K'_{T0}. As can be seen from the fitting results (Table 3), fixing K_{T0}

significantly reduces the uncertainty. From Ne melt to Ab melt, the K_{T0} of the melt generally decreases with increasing SiO_2 fraction, while K'_{T0} increases. The calculated compressional curves based on the fitting results recover the experimental data well (Figure 4). However, its extrapolation to higher pressures is highly uncertain, as the BM-EOS is not based on the physics of liquids and its application to silicate melts is purely empirical.

Another major drawback of applying the BM-EOS to silicate melts is that the compositional dependence of K'_{T0} is not known. Since K'_{T0} is related to the second order derivative of density, a linear mixing model for K'_{T0} is unjustified. Therefore, for each melt composition, an individual K'_{T0} has to be determined from high-P density data, and density data for different melt compositions cannot be combined to derive a single set of equations for all melt compositions. As the composition of silicate melts varies widely in the interiors of the Earth and other planets, it is not possible to measure the density of every melt composition.

3.3. Data Fitting Using the Modified Hard-Sphere EOS (HS-EOS)

Based on the hard-sphere mixture model of liquids (Lebowitz, 1964; Lebowitz et al., 1965), Jing and Karato (2011) proposed a new equation of state for multi-component silicate melts which can well explain the compressional behaviors of silicate melts and their differences with silicate glasses and solids. The model accounts for both entropic and internal energy contributions to compression in silicate melts, in contrast to the BM-EOS which considers only the contribution from internal energy. In this model, each melt component is assigned to a hard sphere of a certain size. Spheres of different sizes representing multiple components move freely in the melt except for the volumes occupied by other spheres. The entropic contribution to compression comes from the geometrical arrangement of these spheres, while the internal energy contribution to compression is provided by the Coulombic attraction between all ions. The temperature dependence of sphere size and sphere deformability were introduced to account for the effect of temperature and pressure on melt properties. Detailed discussion on the formulations of the HS-EOS is given in Jing and Karato (2011). The general form of the HS-EOS is expressed as:

$$P = \frac{\mathrm{RT}}{\overline{V}}\left[(1-\xi)\Phi - \Phi_0\left(\frac{\overline{V}_0}{\overline{V}}\right)^{\mu-1} + \xi\Phi_0\left(\frac{\overline{V}_{m0}}{\overline{V}_m}\right)^{\nu-1}\right], \tag{5}$$

where R is the gas constant, $\overline{V}$ is the molar volume of the melt, $\overline{V}_m$ is the volume of one mol of spheres in the melt. The subscript "0" indicates that a variable is evaluated at room pressure. $\overline{V}_m$ can be written as:

$$\overline{V}_m = \sum_{i=1}^{m} X_i \overline{V}_{\mathrm{mi}} = \frac{1}{6}\pi N_A \sum_{i=1}^{m} X_i \sigma_i^3, \tag{6}$$

where X_i , $\overline{V}_{\mathrm{mi}}$, and σ_i are the concentration, volume of one mol of spheres, and sphere diameter for the i-th melt component, respectively; N_A is the Avogadro constant. The three different terms on the right-hand side of Equation 5 represent the excluded volume effect, the Coulombic attraction, and the repulsive energy contribution due to the deformability of spheres. $\mu = 4/3$ and $\nu = 8/3$ are the exponents for the attractive and repulsive energy terms, respectively. The parameter Φ is a function of the packing fraction ($f = \overline{V}_m/\overline{V}$) and represents the excluded volume effect of the hard spheres. The packing fraction (f) itself also depends on the molar volume of the melt ($\overline{V}$), the composition of the melt (X_i) and the sphere diameter of each melt component (σ_i). The detailed formulation of Φ can be found in Jing and Karato (2011).

The major parameters to calibrate for the HS-EOS are the sphere diameter (σ_i) for each component in the melt and the effect of temperature and pressure on the sphere diameter, which can be evaluated as:

$$\sigma_i = \sigma_{i0,T_{\mathrm{ref}}}\left(\frac{T}{T_{\mathrm{ref}}}\right)^{\eta_i} \exp\left[\frac{\xi_i}{3}\alpha_0(T - T_{ref})\right]\left(\frac{\overline{V}}{\overline{V}_0}\right)^{\frac{\xi_i}{3}}, \tag{7}$$

where $\sigma_{i0,T_{\mathrm{ref}}}$ is the diameter of the sphere at the reference temperature (1,773 K in this study) and room pressure. σ_i is the sphere diameter at high P-T conditions. η_i and ξ_i describe the temperature and volume dependences of the

Table 3
BM-EOS Fitting Results

Composition	K_{T0}	K'_{T0}
Ab	$19.2^{+2.4}_{-6.8}$	$3.8^{+8.2}_{-0.8}$
	17.9 (fixed)	4.8 ± 1.1
Jd	$19.0^{+3.2}_{-7.8}$	$4.0^{+8.9}_{-1.0}$
	19.6 (fixed)	3.6 ± 1.2
Ne	$21.9^{+3.1}_{-7.2}$	$4.7^{+8.3}_{-1.7}$
	24.3 (fixed)	3.0 ± 0.8

Note. Reference T at 1,773 K.

sphere diameter for the i-th component, respectively. The average of the sphere deformability ξ can be expressed as:

$$\xi = \left(\frac{\partial ln\overline{V}_m}{\partial ln\overline{V}}\right)_T = \frac{1}{\overline{V}_m}\sum_{i=1}^{m} X_i\overline{V}_{\mathrm{mi}}\xi_i. \quad (8)$$

When $\xi = 0$, the liquid is a hard-sphere mixture and no sphere deformation occurs, whereas when $\xi = 1$, the liquid will behave like a solid and the entropic contribution to compression will vanish.

The HS-EOS is based on the physical model of the hard-sphere mixtures for liquids, and the effect of composition is explicitly included in the EOS, in contrast to the BM-EOS in which no composition effect is considered. This advantage of the HS-EOS gives us the opportunity to employ all available melt density data for various melt compositions to calibrate a single, unified EOS for silicate melts. All compressional properties of silicate melts at high pressures can be derived from the HS-EOS (Jing & Karato, 2011). In addition, the room-pressure bulk moduli data obtained from ultrasonic measurements can also be incorporated to calibrate the HS-EOS. Taking the volume derivative of Equation 5 and letting $P = 0$, one can obtain the formulation for the room-P bulk modulus as (Jing & Karato, 2011, 2012):

$$K_{T0} = \frac{\mathrm{RT}}{\overline{V}_0}\left[(1-\xi_0)^2\Gamma_0 + \Phi_0\left(2\xi_0 + (\nu-2)\xi_0^2 - \mu\right)\right], \quad (9)$$

where $\Gamma = \partial(f\Phi)/\partial f$. The K_{T0} data can be obtained through ultrasonic sound velocity measurements via:

$$\frac{1}{K_{T0}} = \frac{\overline{V}_0}{c^2} + \frac{T\overline{\mathrm{V}}_0\alpha_0^2}{C_{P0}}, \quad (10)$$

where c is the measured relaxed sound velocity for silicate melts, and α_0 and C_{P0} are the room-pressure thermal expansion coefficient and heat capacity, respectively, which can be calculated from the linear mixing model for silicate melts (Lange, 1997; Lange & Navrotsky, 1992). Therefore, the room-pressure K_{T0} data derived from ultrasonic measurements and the high-P density data obtained from various methods can be combined to fit Equation 5 and Equation 9 simultaneously by minimizing a misfit function:

$$\Delta = \left[\sum\nolimits_j (P_j - P)^2 + \sum\nolimits_k (K_{T0,k} - K_{T0})^2\right], \quad (11)$$

where P_j is the pressure for the j-th density measurement, and $K_{T0,k}$ is the room-P bulk modulus for the k-th bulk modulus measurement.

Our high-P density for Ab, Jd and Ne melts, combined with the room-P bulk modulus data obtained from the ultrasonic measurements of Kress et al. (1988), were employed to calibrate the HS-EOS for the Na_2O-Al_2O_3-SiO_2 (NAS) melt system. Due to the interaction between the Na_2O and the Al_2O_3 components to maintain local charge balance, Jing and Karato (2011) introduced an Na_2O-Al_2O_3 interaction term $c_{\mathrm{Na_2O-Al_2O_3}}$ to account for the compositional dependence of the sphere diameter for the Na_2O component which has an effective sphere diameter expressed as:

$$\sigma'_{\mathrm{Na_2O}} = \sigma_{\mathrm{Na_2O}}(1 + X_{\mathrm{Al_2O_3}}c_{\mathrm{Na_2O-Al_2O_3}}). \quad (12)$$

Introducing such an interaction term can significantly improve the fitting for Na_2O-bearing melts (Jing & Karato, 2011). Therefore, we have also adopted the interaction term for Na_2O-Al_2O_3 in our calibration. Our high-P density data on NAS melts provides significantly better constraints on the parameters for the Na_2O component compared to the previous calibration by Jing and Karato (2011), in which only 1-atm density and bulk modulus data were incorporated for the Na_2O-bearing melts. In total, 38 relaxed bulk moduli data from Kress et al. (1988)

Table 4
Calibrated Sphere Diameters and Their Temperature and Volume Dependences for the NAS Melt System

Component	$\sigma_{i0,T_{ref}}$ (nm)	η_i	ξ_i
SiO_2	0.370 ± 0.018	−0.11 ± 0.03	0.91 ± 0.36
Al_2O_3	0.447 ± 0.046	0.13 ± 0.07	1.00 ± 0.84
Na_2O	0.371 ± 0.042	−0.10 ± 0.11	0.34 ± 0.48
$c_{Na_2O-Al_2O_3}$	0.12 ± 0.73[a]		

Note. T_{ref} is 1773 K, and errors are 1 σ estimates. [a]The interaction term is a non-dimensional parameter.

and 24 density measurements from our study were used in the calibration. A non-linear regression was conducted on these data by minimizing Equation 11. Our calibrated sphere diameters and their temperature and volume dependences for the NAS melts are listed in Table 4. The calculated compressional curves using the calibrated HS-EOS recover the experimental density data well (Figure 4). Compared to the BM-EOS, the HS-EOS predicts similar density results for the NAS melts at low pressures, but slightly higher densities at higher pressures, implying a higher melt compressibility captured by the HS-EOS.

The calibrated parameters for the HS-EOS have relatively large uncertainties (Table 4) due to the large number of parameters involved and the limited *P-T* range for the experimental data. We therefore conducted another calibration using an average sphere deformability (Equation 8) for the NAS melts. The new calibration results are shown in Table 5 with significantly reduced uncertainties. The density results can also be well reproduced by using a single ξ for the melts (Figure 4), although fewer parameters were employed for the HS-EOS. The predicted room-pressure bulk modulus K_{T0} (Equation 9) and density ρ (Equation 5) using both calibrations can match the experimental data equally well, with a residual in percentage less than 2% and 1.5%, respectively (Figure 5). Therefore, the HS-EOS with an average ξ is recommended for calculating the density for NAS melts at high *P-T* conditions up to ~5 GPa and 2000 K. It should be noted that the bulk moduli data from Kress et al. (1988) contain multiple measurements on same compositions at roughly same conditions, thus being shown as arrayed horizontal segments with a range of experimental K_{T0} values corresponding to a constant calculated K_{T0} value (Figure 5a). This is purely due to the repeatability uncertainty associated with the experiments and does not mean that the variability in K_{T0} is not captured by the HS-EOS.

3.4. Extending the HS-EOS to Silicate Melts in the CaO-MgO-Al_2O_3-SiO_2-FeO-Na_2O-K_2O (CMASFNK) System

Here we combine our new high-P density data on sodium aluminosilicate melts with other high-P density data and room-P sound velocity data for a wide range of melt compositions from the literature to calibrate a universal EOS for silicate melts in the CAMSFNK system, covering nearly all the major components in silicate melts except for TiO_2 and volatiles. The data sources used in the calibration are compiled in SI Table S1 in Supporting Information S1, including the data set originally compiled by Jing and Karato (2011) together with some more recent sound velocity and density measurements on various melt compositions. The room-P sound velocity data from Ai and Lange (2008) Guo et al. (2013), Guo et al. (2014), Kress et al. (1988), Rivers and Carmichael (1987), Secco et al. (1991), and, Webb and Courtial (1996) combined with the linear mixing models for the molar volume, thermal expansivity, and heat capacity of silicate melts at room pressure (Lange, 1997; Lange & Carmichael, 1987; Lange & Navrotsky, 1992) were used to calibrate the room-P bulk modulus K_{T0} in Equation 9. Only the sound velocity data that can be confirmed to be relaxed, that is, showing no frequency dependence, were used in the calibration. High-P density data include the sink-float/X-ray absorption experimental results on volatile-free silicate melts from Agee (1998), Agee and Walker (1993), Ohtani and Maeda (2001), Sakamaki et al. (2010), Suzuki and Ohtani (2003), and Suzuki et al. (1998), as compiled in Jing and Karato (2011), Jing and Karato (2012), and more recent data from X-ray absorption measurements on relatively silica-rich melt compositions (Malfait, Seifert, Petitgirard, Mezouar, et al., 2014; Malfait, Seifert, Petitgirard, Perrillat, et al., 2014; Seifert et al., 2013), as well as the 24 data points from this study on sodium aluminosilicate melts determined from X-ray microtomography. Compared to other density models (e.g., Ueki & Iwamori, 2016), the current HS-EOS calibration has the most extensive data set, covering both the relaxed sound velocity data and the high-P density data on volatile-free silicate melts in the literature to date.

Table 5
Calibrated Sphere Diameters and Their Temperature and Volume Dependences for the NAS Melt System Using an Average Sphere Deformability

Component	$\sigma_{i0,T_{ref}}$ (nm)	η_i	ξ
SiO_2	0.370 ± 0.001	−0.06 ± 0.02	0.67 ± 0.03[a]
Al_2O_3	0.439 ± 0.008	0.13 ± 0.05	
Na_2O	0.370 ± 0.004	−0.14 ± 0.02	
$c_{Na_2O-Al_2O_3}$	0.16 ± 0.11[b]		

Note. T_{ref} is 1,773 K, and errors are 1 σ estimates. [a]ξ is the average of sphere deformability and takes the same value for all melt components. [b]The interaction term is a non-dimensional parameter.

A regression was conducted on the data set in Table S1 in Supporting Information S1 using Equations 5 and 9 simultaneously by minimizing Equation 11. The matlab code used for performing the HS-EOS fitting has been provided in the data repository (Xu et al., 2025). The calibrated sphere

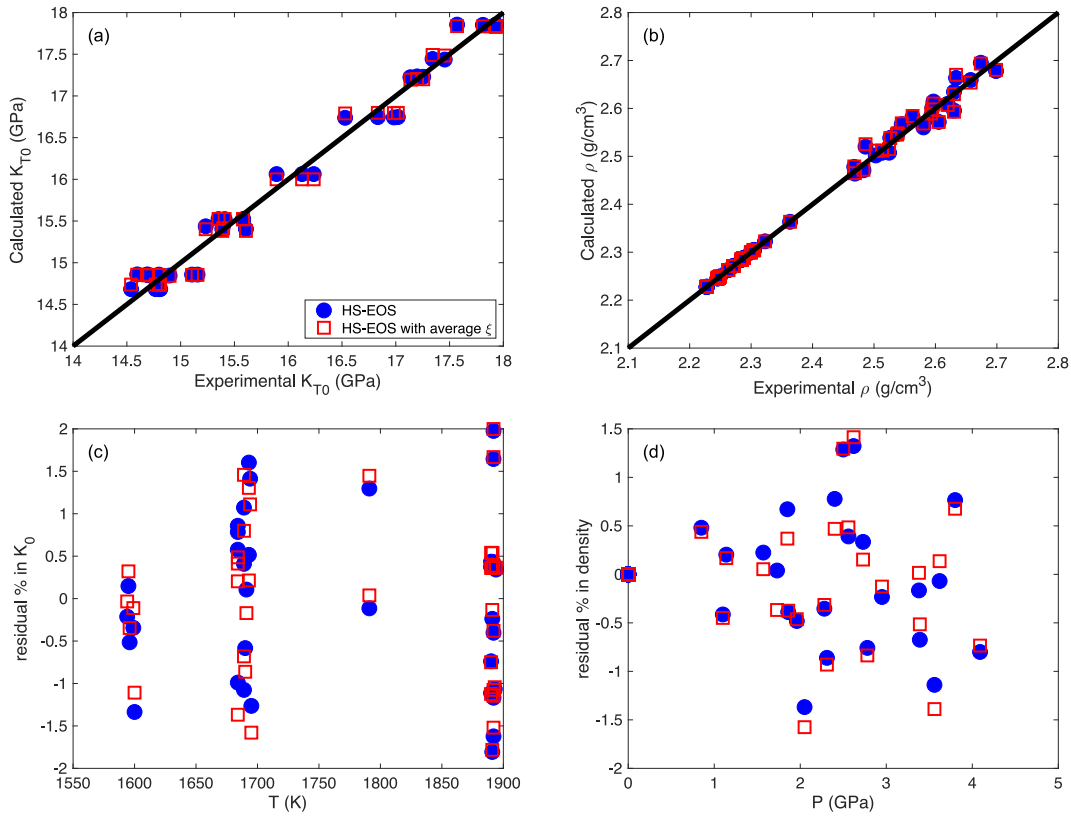

Figure 5. (a) Calculated K_{T0} versus experimental K_{T0}, and (b) calculated ρ versus experimental ρ based on the calibrated hard-sphere equation of state (HS-EOS) with individually defined sphere deformability ξ_i (Table 4, blue circles) and HS-EOS with an average sphere deformability ξ (Table 5, red squares) using Equation 9 and Equation 5, respectively. The black line shows the 1:1 correlation between the axes. (c) Residual in percentage for the calculated room-pressure bulk moduli as a function of temperature. (d) Residual in percentage for the calculated densities as a function of pressure.

parameters for each component are listed in Table 6. The uncertainty in the K_2O component is relatively large due to the very limited number of data points on K_2O-bearing silicate melts at both room P and high P (Table S1 in Supporting Information S1). More data on K_2O-rich melts are needed in future to better constrain the parameters for the K_2O component. The fitted sphere diameters are generally consistent with those obtained in Jing and Karato (2011) for the CMASF system. It should be noted that the Al_2O_3 component in the previous calibration by Jing and Karato (2011) was treated as $AlO_{1.5}$ during the regression. Therefore, their fitted sphere diameter for Al_2O_3 should be about a factor of $\sqrt[3]{2} = 1.26$ smaller than that of the present calibration. The calculated K_{T0} and density ρ using the calibrated parameters in Table 6 recover the experimental values very well (Figure 6, blue circles), with the maximum residuals for K_{T0} less than 8% (~2 GPa) and for ρ better than 3%. For most melt compositions, the difference between the calculated densities using the HS-EOS and the experimental values is smaller than 2%. Therefore, the current calibrated HS-EOS can be confidently applied to calculate the high-P density of silicate melts in the CMASFNK system. We have also conducted another regression using an average sphere deformability ξ for the HS-EOS, and the calibration results are shown in Table 7. Although the calibration using an average sphere deformability can also fit the experimental data very well, the residuals are slightly larger than the calibration using the regular HS-EOS. As the fitting of separate ξ_i for each component does not result in very large uncertainties in the calibrated parameters, the regular HS-EOS is thus recommended for calculating the densities for melts in the CAMSFNK system

Table 6
Calibrated Sphere Diameters and Their Temperature and Volume Dependences for the CAMSFNK Melt System

Component	$\sigma_{i0,T_{ref}}$ (nm)	η_i	ξ_i
SiO_2	0.358 ± 0.001	−0.09 ± 0.01	0.39 ± 0.02
Al_2O_3	0.426 ± 0.001	−0.01 ± 0.01	0.66 ± 0.03
MgO	0.287 ± 0.002	0.16 ± 0.01	0.71 ± 0.07
CaO	0.340 ± 0.001	0.00 ± 0.01	0.91 ± 0.03
FeO	0.255 ± 0.002	0.03 ± 0.01	−0.46 ± 0.09
Na_2O	0.361 ± 0.010	0.01 ± 0.01	0.34 ± 0.19
K_2O	0.440 ± 0.113	0.04 ± 0.08	0.69 ± 0.37
$c_{Na_2O-Al_2O_3}$	0.29 ± 0.03[a]		

Note. T_{ref} is 1,773 K, and errors are 1 σ estimates. [a]The interaction term is a non-dimensional parameter.

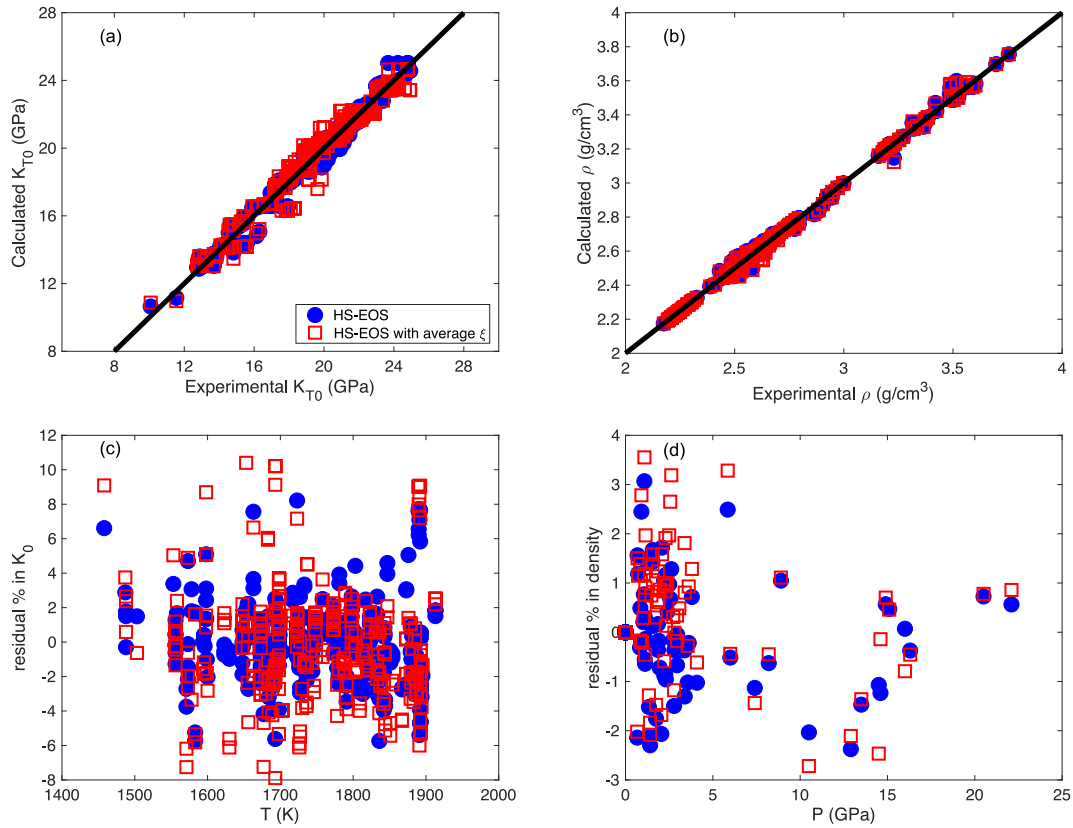

Figure 6. (a) Calculated K_{T0} versus experimental K_{T0}, and (b) calculated density ρ versus experimental ρ based on the calibrated hard-sphere equation of state (HS-EOS) with individually defined sphere deformability ξ_i (Table 6, blue circles) and HS-EOS with an average sphere deformability ξ (Table 7, red squares) for CAMSFNK melt system using Equation 9 and Equation 5, respectively. The black line shows the 1:1 correlation between the axes. (c) Residual in percentage for the calculated room-pressure bulk moduli as a function of temperature. (d) Residual in percentage for the calculated densities as a function of pressure.

Table 7
Calibrated Sphere Diameters and Their Temperature and Volume Dependences for the CAMSFNK Melt System Using an Average Sphere Deformability

Component	$\sigma_{i0,T_{ref}}$ (nm)	η_i	ξ
SiO_2	0.359 ± 0.001	−0.11 ± 0.01	0.43 ± 0.02[a]
Al_2O_3	0.417 ± 0.001	−0.07 ± 0.01	
MgO	0.278 ± 0.001	0.18 ± 0.01	
CaO	0.321 ± 0.001	0.13 ± 0.02	
FeO	0.280 ± 0.001	−0.11 ± 0.01	
Na_2O	0.368 ± 0.001	0.06 ± 0.02	
K_2O	0.429 ± 0.003	0.15 ± 0.08	
$c_{Na_2O-Al_2O_3}$	0.21 ± 0.01[b]		

Note. T_{ref} is 1773 K, and errors are 1 σ estimates. [a]ξ is the average of sphere deformability and takes the same value for all melt components. [b]The interaction term is a non-dimensional parameter.

up to ~25 GPa and 2,000 K. For Na_2O-rich melts, although our own experimental data only extend to 4.1 GPa, the extrapolation using our HS-EOS to 25 GPa is unlikely to result in a significant increase in the uncertainty. This is because that the effect of pressure is mainly described by the sphere deformability parameter ξ_i in the HS-EOS model, which can be treated as a constant up to ~40 GPa (Jing & Karato, 2011). For K_2O-rich melts, due to limited data set, the calibrated parameters have relatively large uncertainties, and their extrapolation using our HS-EOS model should be treated with caution. Future measurements on a wider composition range at much higher pressures are needed to better refine the HS-EOS.

Compared to the previous studies (Jing & Karato, 2011, 2012), the main contribution of current study to the HS-EOS is to extend its applicability to a larger compositional space. Due to the lack of high-P density data on Na_2O-bearing melts, the previous studies did not constrain the volume dependence of the sphere diameter ξ_i for the Na_2O component. Our new data and calibration provide constraints on all the HS-EOS parameters related to the Na_2O component. While K_2O was also included in our calibration, its uncertainty is relatively large due to limited data. Therefore, our new calibration is more suitable for modeling alkali-rich melts, particularly for sodium-bearing melts in planetary interiors.

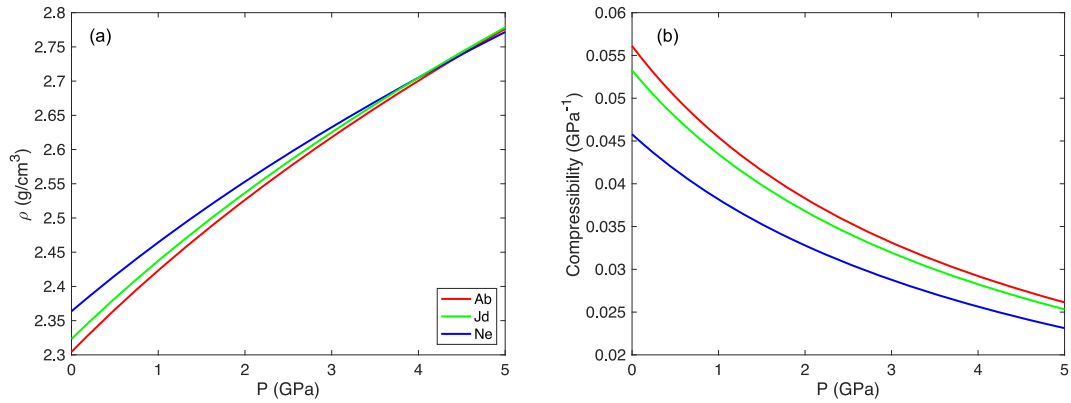

Figure 7. (a) Density and (b) compressibility as a function of pressure for Ab-Jd-Ne melt join calculated at the reference temperature 1773 K using the modified hard-sphere equation of state (Table 5).

4. Discussion

4.1. Effect of Composition on Melt Compressibility and Density

The composition of a silicate melt plays an important role in determining its properties. Figure 7 compares the density and compressibility for melts on the Ab-Ne join calculated using our modified HS-EOS. The results suggest that with greater $NaAlO_2$ substitution for SiO_2 along this join, the density increases while the compressibility decreases. This is consistent with the room-pressure sound velocity measurements showing that the melt velocity increases with increasing Na_2O content in Na_2O-Al_2O_3-SiO_2 melts (Kress et al., 1988). Structural measurements on polymerized silicate melts have shown that the dominant compression mechanism in relatively low-pressure range is through bending and tightening of the inter-tetrahedral bond angles (Wang et al., 2014). It has been suggested that the effect of the substitution of $(NaAl)^{4+}$ for Si^{4+} is to narrow the T-O-T bond angle (where T represents the tetrahedrally coordinated cations) (Okuno & Marumo, 1982), as T-O-T linages containing Al^{3+} would carry electric charges, providing an electrostatic attraction between the Al-containing tetrahedra and alkali cations (Navrotsky et al., 1985). For fully polymerized melts along the Ab-Ne join, Al^{3+} is expected to be a network former in the tetrahedral site, and Na^+ would show greater structural affinity to the T-O-Al bridges, perturbing the Al-O bond more than the Si-O bond. Therefore, replacing Si^{4+} with $(NaAl)^{4+}$ is expected to narrow and restrict the T-O-T angles, resulting in its lower compressibility with increasing $(NaAl)^{4+}$ content. However, it should be noted that this may only hold true when Al^{3+} in the melt is a network former. For compositions with $Al_2O_3 > Na_2O$, Al^{3+} is likely to become a network modifying cation with a substantial portion entering the six-fold coordinated sites (Mysen et al., 1980), which may show different trends than those along the Ab-Jd-Ne join.

Due to the complex structures and interactions among different components in multi-component silicate melts, it is difficult to find a single parameter to characterize the effect of composition on melt properties. Here our calibrated HS-EOS were employed to evaluate the general trend for each individual component on the elastic properties of silicate melts. The calculated K_{T0} for various melt compositions (Table S1 in Supporting Information S1) are plotted as a function of the mole fraction of the individual oxide component in Figure 8. The bulk moduli generally demonstrate a decreasing trend with increasing SiO_2 and alkali contents, an increasing trend with CaO content, and are nearly independent of the MgO, FeO, and Al_2O_3 contents in the melts. It seems that SiO_2, alkalis, and CaO are the major components contributing to the compositional dependence of melt elastic properties. All these components have relatively large sphere diameters (>0.3 nm) (Table 6), while components with small sphere diameters (FeO, MgO) seem to play a less important role. Al_2O_3 is an outlier, likely due to its dual role in melt structures, either as a network former or a network modifier, which may help compensate its compositional effect. The trend for SiO_2 is consistent with structural measurements on silicate melts (Wang et al., 2014), showing that before reaching the tetrahedral packing limit, polymerized melt will be depolymerized (breakup of the tetrahedral connectivity) first upon compression through tightening of the inter-tetrahedral bond angles, resulting in its high compressibility. It is interesting to see that although both alkalis and CaO tend to act as network modifiers in silicate melts, their general trends are totally different. Increasing the number of interstitial ions within the tetrahedral network will generally

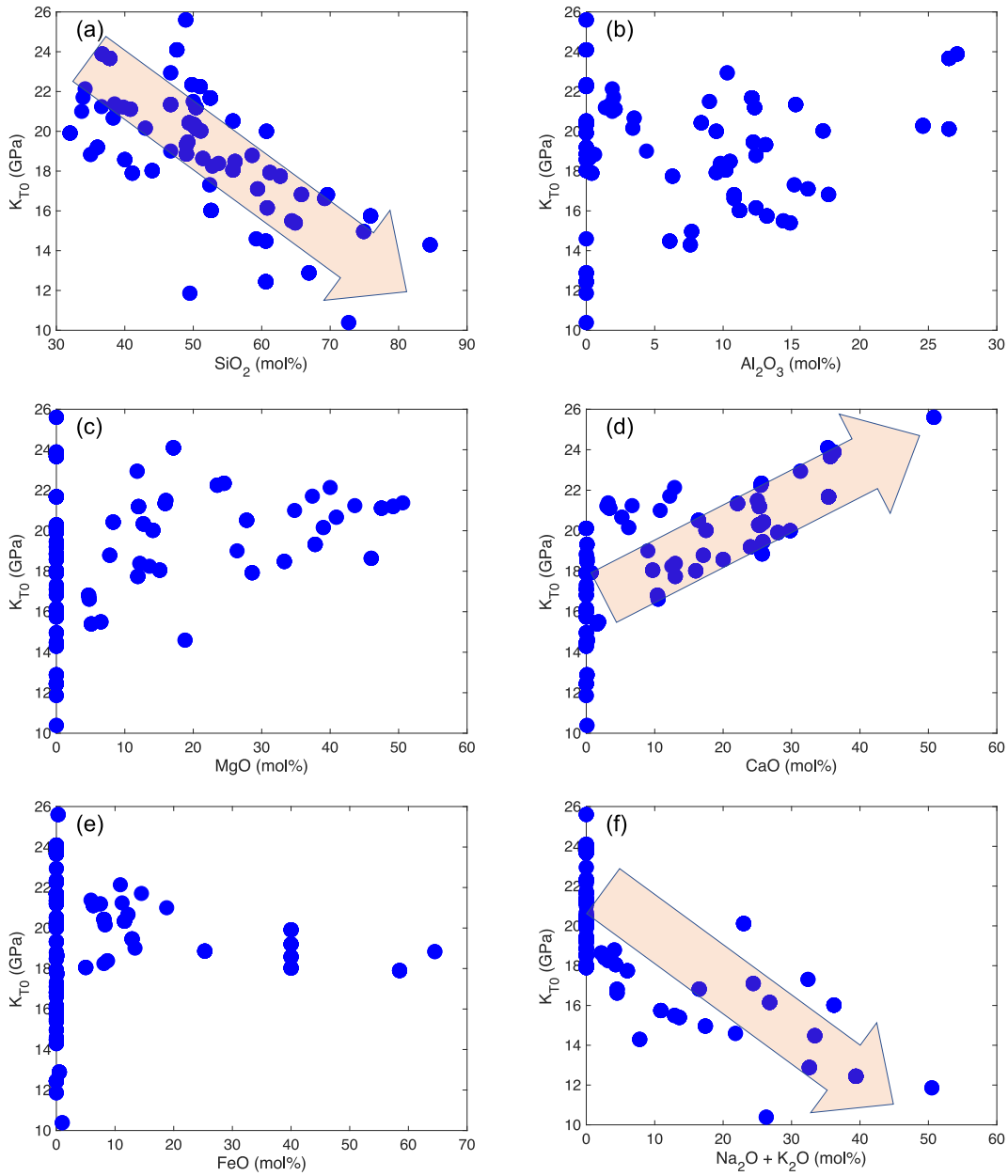

Figure 8. Calculated K_{T0} using the hard-sphere equation of state for various melts as a function of (a) SiO_2 content, (b) Al_2O_3 content, (c) MgO content, (d) CaO content, (e) FeO content, and (f) total alkali ($Na_2O + K_2O$) content.

reduce free space, and is thus expected to result in lower compressibility of the melt, as is the case for CaO. The effect of alkalis on melt properties is more complicated. On one hand, alkali-rich melts also tend to be silica rich in most cases, so their effects are likely coupled together. On the other hand, alkali ions have lower charge and larger sizes than alkaline earth ions, which may lead them to have greater disruption of the network connectivity (Karlsson et al., 2005), resulting in more non-bridging oxygens and higher compressibility. The calibrated partial molar compressibilities by room-pressure ultrasonic measurements for the two alkali components are also higher than that of other components (Rivers & Carmichael, 1987), supporting the important role of alkali components in modifying the elastic properties of silicate melts. A general simplified conclusion from observing Figure 8 is that alkali-rich, polymerized melts are generally more compressible than alkali-poor, depolymerized ones. It should be noted that this general observation cannot be directly applied to a specific melt composition, as outliers from this general trend do exist, such as the case for Ab-Jd-Ne join.

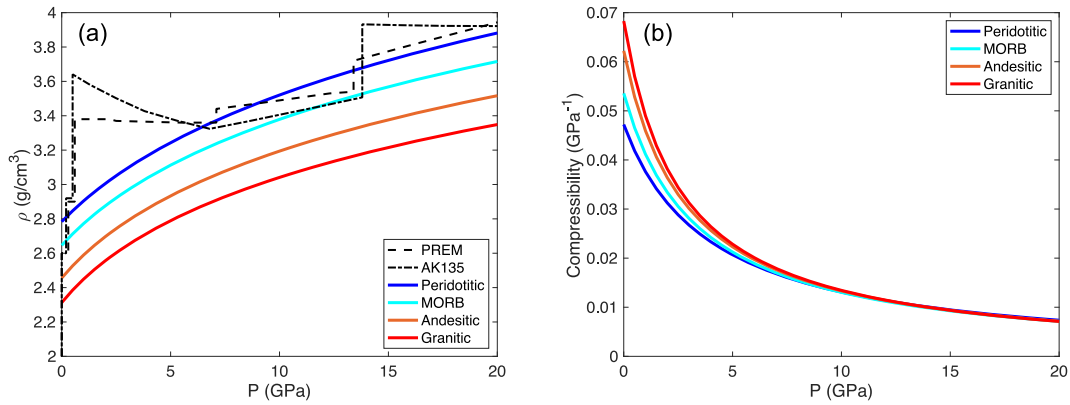

Figure 9. Calculated (a) density and (b) compressibility as functions of pressure for some representative silicate melt compositions using the hard-sphere equation of state model. The melt compositions include peridotite (blue), tholeiitic basalt (MORB) (cyan), andesite (orange), and peralkaline granite (red) from Rogers (2015). PREM (dash line) and AK135 (dash-dot line) are from Dziewonski and Anderson (1981) and Kennett and Engdahl (1991), respectively.

We have further calculated the compressibility and density as functions of pressure for some representative silicate melt compositions on Earth using our calibrated HS-EOS, including peridotitic, MORB (tholeiitic), andesitic, and granitic melts in Figure 9. The representative melt compositions are from Rogers (2015). As expected, the density of peridotitic melt is the highest while the density of granitic melt is the lowest in Earth's interior. Compared to the PREM (Dziewonski & Anderson, 1981) and AK135 model (Kennett & Engdahl, 1991), only peridotitic and MORB melts could have density crossovers with the solid mantle, at ∼7–9 and ∼12 GPa, respectively (Figure 9a). Melts with andesitic and granitic compositions should be always positively buoyant relative to the ambient mantle despite their higher compressibility. Our results indicate that even though increasing SiO_2 in the melt can significantly increase the melt compressibility, such effect is only pronounced in the low-pressure range (<10 GPa) and rapidly diminishes with increasing pressure. This is likely due to the fact that SiO_2-rich, polymerized melts have a "spongier" initial intermediate-range structure than depolymerized melts (Sakamaki et al., 2014; Wang et al., 2014). In the low-pressure range, the compression of polymerized melts is mostly accommodated through bending and tightening of the T-O-T angles and compaction of voids in the intermediate range structure, resulting in their high compressibility. With further increasing pressure, the tetrahedral packing limit is reached, and Si, Al coordination changes start to play a dominate role in accommodating the compression (Wang et al., 2014).

4.2. Implications for the Stability of Alkali Basaltic Melt at the Continental lithosphere-asthenosphere boundary (LAB)

The lithosphere-asthenosphere boundary (LAB) beneath continents is a key discontinuity bearing on the origin and evolution of continents and their dynamics (Aulbach et al., 2017; Fischer et al., 2010). It is characterized by strong seismic velocity gradients and enhanced electrical conductivity, which may require the presence of partial melts (Eaton et al., 2009; Jones, 1999; Yuan & Romanowicz, 2010). A previous study suggested that alkali basaltic magmas could be gravitationally trapped at the continental LAB, providing a way to explain its geophysical characteristics (Crépisson et al., 2014). However, the density measurements by Crépisson et al. (2014) on alkali basaltic melt may have suffered from several experimental limitations and assumptions. First, because the study by Crépisson et al. (2014) relied on a combination of challenging X-ray diffraction and absorption measurements to determine the density of alkali basaltic melts, only two experimental runs were performed, both at sub-liquidus conditions. Fully molten of the sample is not guaranteed and the presence of small residual crystals in the melt at sub-liquidus conditions may have complicated the absorption and diffraction measurements, thereby affecting the density results. In addition, the derived equation of state for alkali basaltic melt has large uncertainties due to the small number of data points (only two) and the presence of volatiles with poorly constrained partial molar properties. Therefore, its extrapolation to higher pressure is debatable.

Here, using our newly calibrated HS-EOS model for multi-component silicate melts, we have reevaluated the gravitational stability of alkali basaltic melt at the continental LAB conditions. The alkali basaltic melt composition

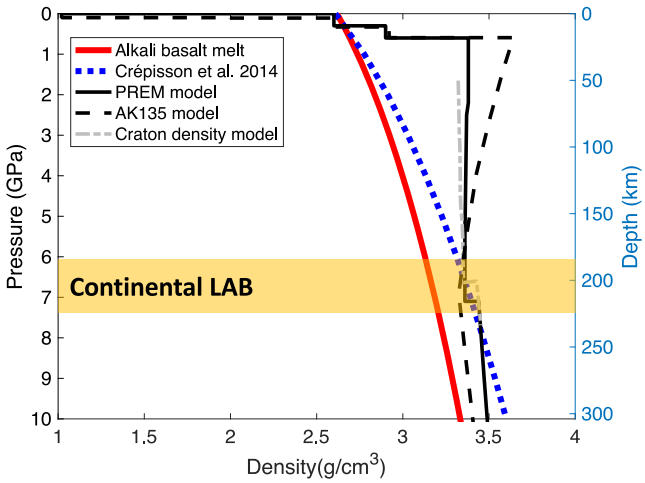

Figure 10. Density of alkali basaltic melt (red curve) as a function of pressure and depth calculated using the hard-sphere equation of state along a mantle adiabat (Katsura, 2022) and its comparison with the previous density measurements by Crépisson et al. (2014) (blue dotted curve), the PREM model (Dziewonski & Anderson, 1981) (black solid curve), the AK135 model (Kennett & Engdahl, 1991) (black dashed curve) and a cratonic mantle density model (Poudjom Djomani et al., 2001) (gray dash-dot curve). The shaded area marks the approximate depth range for the continental Lithosphere-asthenosphere Boundary.

used in our calculations is the same as that of the starting material used in Crépisson et al. (2014), with the composition originally reported in Pichavant et al. (2009). In contrast to the previous study (Crépisson et al., 2014), our new results suggest that alkali basaltic melts are positively buoyant relative to the cratonic mantle (Figure 10). It should be noted that the calculation represents a minimum buoyancy scenario, as our HS-EOS is calibrated for volatile-free compositions and the presence of dissolved volatiles would significantly lower melt density (e.g., Jing & Karato, 2012), which could further increase its buoyancy. Therefore, typical alkali basaltic melts should migrate upward to metasomatize the deep cratonic root. Due to the good wetting properties of basaltic melts (Holness, 2006; Yoshino et al., 2009), compaction and percolation may cause the melt at the LAB to drain even at small melt fractions (Faul, 2001; McKenzie, 1985). This may help explain the sparseness of seismic observations of the continental LAB due to the difficulty of retaining melts beneath these thick (200–250 km) regions of lithosphere (Aulbach et al., 2017). For cratons where clear LABs are seismically imaged (Ford et al., 2010; Foster et al., 2014; Rychert et al., 2005), other mechanisms such as ponded melts due to the pressure-induced change in melt viscosity and mobility (Sakamaki et al., 2013; Zhou et al., 2024) or long-lived mantle upwellings to replenish the melts (Zhao et al., 2015) must be invoked to explain their long-term presence at the continental LAB. For most of the cratonic mantle, our results support the view that melt migration and percolation from the LAB upwards lead to the thermochemical erosion of the cratonic roots, thereby generating the topography at the LAB (non-flat LAB at various depths) and its weak, intermittent seismic signals (Aulbach et al., 2017). These weak continental LABs may reflect ongoing melt-lithosphere interaction.

4.3. Implications for Melt Extraction Processes in Planetesimals

Recent discoveries of andesitic meteorites have suggested that the products of early silicate melting in planetesimals are silica- and alkali-rich in nature (Barrat et al., 2021; Bischoff et al., 2014; Nicklas et al., 2022). This has been supported by melting experiments on chondritic materials, showing that silica- and alkali-rich melts can be widely produced during low-degree (<15%) planetesimal melting (Collinet & Grove, 2020; Lunning et al., 2017; Usui et al., 2015). Such melts have compositions that resemble those of igneous andesitic or trachyandesitic achondrites, with the residual mineral assemblages similar to those of primitive achondrites (Collinet & Grove, 2020). These silicic, alkali-rich melts are highly viscous, with viscosities larger than 10^3 Pa s (Giordano et al., 2008), and are thought to be unable to efficiently extract through melt compaction and percolation (Collinet & Grove, 2020; Monnereau et al., 2023). The calculations by Collinet and Grove (2020) suggest that such high-viscosity melts can only migrate a negligible distance compared to the radius of even the smallest planetesimals over the timescale of one half-life of ^{26}Al (0.72 Ma). This means that a planetesimal would either be melted into a magma ocean, if sufficient ^{26}Al was present at the time of accretion, or it would cool below the solidus too rapidly to migrate significantly due to depletion of the radiogenic heat source after low-degree partial melting (Lichtenberg et al., 2019; Zhang et al., 2023). In either case, the removal of low-degree silica- and alkali-rich melts recorded by the formation of andesitic and primitive achondrites is difficult to explain. Alternatively, Collinet and Grove (2020) proposed that migration of such viscous melts in planetesimals may be similar to the silicic melts on Earth, with excess pressures in the magma chamber leading to the formation of veins and dykes that can significantly increase the drainage efficiency of the partial melts (Sleep, 1988). The excess pressure may come from the large density contrast between the melts and wall rocks (Malfait, Seifert, Petitgirard, Perrillat, et al., 2014) and/or exsolution of volatiles from the magma (Sisson & Bacon, 1999). However, whether this overpressure is large enough to initiate cracks and veins in planetesimals has not been quantitatively evaluated.

Here using our HS-EOS model, we can evaluate the buoyancy-driven overpressure for silica- and alkali-rich melts in planetesimals. We use the composition of recently identified andesitic achondrite Erg Chech (EC) 002 (Nicklas et al., 2022) as the representative composition for low-degree silica- and alkali-rich silicate melts in planetesimals. Assuming that the gravity on planetesimals can be scaled as $g = (g_E R)/R_E$, where R represents the radius of the

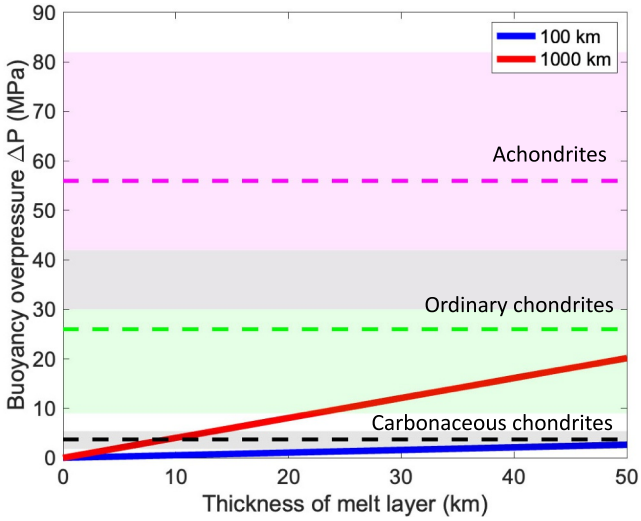

Figure 11. Calculated buoyancy overpressure for silica- and alkali-rich early melts in planetesimals using our hard-sphere equation of state. The melt composition is from andesitic achondrite EC002 (Nicklas et al., 2022), and the density and temperature of planetesimal are assumed to be 3,300 kg/m^3 and 1400 K, respectively (Moskovitz & Gaidos, 2011). The tensile strength for various meteorites is from the compilation of Pohl and Britt (2020), with the black, green and magenta dashed lines correspond to the average values for carbonaceous chondrites, ordinary chondrites and achondrites, respectively, and the shaded areas correspond to the possible ranges for each category of meteorites.

planetesimal and subscript E refers to the Earth (Solferino et al., 2020), we can calculate the buoyancy-driven overpressure ΔP due to the production of these melts by integrating the density contrast $\Delta\rho$ between the melt and surrounding rock over the thickness of the melt layer (dz), with $\Delta P = g/2 \int \Delta\rho dz$ (Malfait, Seifert, Petitgirard, Perrillat, et al., 2014). Figure 11 shows the results calculated for a 100 and 1,000 km radius planetesimal, respectively, and their comparison with the average tensile strength of chondritic and achondritic meteorites (Pohl & Britt, 2020). For a planetesimal with 100 km radius, the buoyancy overpressure created by the silica- and alkali-rich melts only becomes comparable to the average tensile strength of carbonaceous chondrites when the melt layer is more than 40 km thick, and are always much smaller than the strength of ordinary chondrites (Figure 11). In contrast, for a 1,000 km planetesimal, the buoyancy overpressure can exceed the strength of carbonaceous chondrites and becomes comparable to the strength of ordinary chondrites when the thickness of the melt layer exceeds ~20 km. However, even for 1,000 km planetesimals the buoyancy overpressure is significantly smaller than the tensile strength of achondrite, which is thought to be the differentiated product in planetesimals after melt removal. Therefore, our results suggest that the buoyancy overpressure may play a negligible role in extracting early silica- and alkali-rich melts in planetesimals, as it is not large enough compared to the tensile strength of solid matrix to initiate veins and dykes (Collinet & Grove, 2020). It may contribute to the melt extraction processes for larger planetesimals and planetesimals made of carbonaceous chondritic materials, but it is unlikely to be the dominant mechanism. Other mechanisms such as the recently proposed "rubble-pile" model for melt migration through macropores between meter-sized boulders created by collision and shattering of the planetesimal must be invoked to explain the efficient migration and extraction of these highly viscous melts (Zhang et al., 2023).

5. Conclusions

We have determined the high P-T density of $NaAlSiO_4$, $NaAlSi_2O_6$, and $NaAlSi_3O_8$ melts up to 4.1 GPa and 2,020 K using the high-pressure X-ray microtomography technique in a Paris-Edinburgh cell assembly. The experimental results show that increasing the amount of Si^{4+} at the expense of $(NaAl)^{4+}$ in the melt along the Ab-Ne join will result in lower melt density and higher melt compressibility. The new data were combined with a wide range of literature data on the density and sound velocity of silicate melts with various compositions to calibrate a single, unified equation of state for multi-component silicate melts based on the modified hard-sphere mixture model (Jing & Karato, 2011). Our calibration results can recover the existing density and bulk moduli data for silicate melts to better than 3% and 8%, respectively. This HS-EOS model for silicate melts, incorporating the effects of pressure, temperature, and composition, can be applied broadly in modeling the evolution and dynamics of early Earth and planets. Applying it to alkali basaltic melts at continental LAB conditions shows that alkali basaltic melts are buoyant under these conditions and will tend to migrate upwards to metasomatize the cratonic roots, which may help explain the topography and weak seismic observations of the continental LABs. Our HS-EOS model was also employed to evaluate the buoyancy overpressure generated by silica- and alkali-rich early silicate melts in planetesimals and the results suggest that dyke formation due to buoyancy overpressure is unlikely to be the major mechanism for efficiently extracting melts in planetesimals.

Conflict of Interest

The authors declare no conflicts of interest relevant to this study.

Data Availability Statement

Data associated with this paper are available in Mendeley Data repository (Xu et al., 2025) (https://doi.org/10.17632/gr892kdjt5.1).

Acknowledgments
This research is supported by the National Key Research and Development Program of China (2024YFF0807401) and the Shanghai Pujiang Program (24PJA095) to M. Xu, the National Natural Science Foundation of China (92479108) to Z. Jing, and the US National Science Foundation (EAR-2246803) to Y, Wang. Q. Hu acknowledges the funding support from the National Natural Science Foundation of China (42150101). The experimental work was performed at GeoSoilEnviroCARS (The University of Chicago, Sector 13), APS, Argonne National Laboratory. GeoSoilEnviroCARS (GSECARS) is supported by the National Science Foundation—Earth Sciences via SEES: Synchrotron Earth and Environmental Science (EAR–2223273). This research used resources of the Advanced Photon Source (APS), and the SEM analysis was performed at the Center for Nanoscale Materials (CNM), both are U.S. Department of Energy (DOE) Office of Science User Facilities operated for the DOE Office of Science by Argonne National Laboratory under Contract No. DE-AC02-06CH11357. The authors thank two anonymous reviewers for their constructive comments that help improve this paper.

References

Agee, C. B. (1998). Crystal-liquid density inversions in terrestrial and lunar magmas. *Physics of the Earth and Planetary Interiors*, *107*(1–3), 63–74. https://doi.org/10.1016/S0031-9201(97)00124-6

Agee, C. B., & Walker, D. (1993). Olivine flotation in mantle melt. *Earth and Planetary Science Letters*, *114*(2–3), 315–324. https://doi.org/10.1016/0012-821X(93)90033-6

Ai, Y., & Lange, R. A. (2008). New acoustic velocity measurements on CaO-MgO-Al_2O_3-SiO_2 liquids: Reevaluation of the volume and compressibility of $CaMgSi_2O_6$-$CaAl_2Si_2O_8$ liquids to 25 GPa. *Journal of Geophysical Research*, *113*, B04203. https://doi.org/10.1029/2007JB005010

Aulbach, S., Massuyeau, M., & Gaillard, F. (2017). Origins of cratonic mantle discontinuities: A view from petrology, geochemistry and thermodynamic models. *Lithos*, *268–271*, 364–382. https://doi.org/10.1016/j.lithos.2016.11.004

Barrat, J.-A., Chaussidon, M., Yamaguchi, A., Beck, P., Villeneuve, J., Byrne, D. J., et al. (2021). A 4,565-My-old andesite from an extinct chondritic protoplanet. *Proceedings of the National Academy of Sciences*, *118*(11), 1–7. https://doi.org/10.1073/pnas.2026129118

Bass, J. D., Liebermann, R. C., Weidner, D. J., & Finch, S. J. (1981). Elastic properties from Acoustic and volume compression experiments. *Physics of the Earth and Planetary Interiors*, *25*(2), 140–158. https://doi.org/10.1016/0031-9201(81)90147-3

Bell, P. M., & Roseboom, E. H. J. (1969). Melting relations of jadeite and albite to 45 kilobars with comments on melting diagrams of binary systems at high pressures. *Mineral. Soc. Amer., Spec. Pap. (Mineralogical Society of America Special Paper 2)*, *161*, 151–161.

Birch, A. F., & LeComte, P. (1960). Temperature-pressure plane for albite composition. *American Journal of Science*, *258*(3), 209–217. https://doi.org/10.2475/ajs.258.3.209

Birch, F. (1947). Finite elastic strain of cubic crystals. *Physical Review*, *71*(11), 809–824. https://doi.org/10.1103/PhysRev.71.809

Bischoff, A., Horstmann, M., Barrat, J.-A., Chaussidon, M., Pack, A., Herwartz, D., et al. (2014). Trachyandesitic volcanism in the early solar system. *Proceedings of the National Academy of Sciences*, *111*(35), 12689–12692. https://doi.org/10.1073/pnas.1404799111

Blundy, J., & Dalton, J. (2000). Experimental comparison of trace element partitioning between clinopyroxene and melt in carbonate and silicate systems, and implications for mantle metasomatism. *Contributions to Mineralogy and Petrology*, *139*, 356–371. https://doi.org/10.1007/s004100000

Boettcher, A. L., Burnham, C. W., Windom, K. E., & Bohlen, S. R. (1982). Liquids, glasses, and the melting of silicates to high pressures. *The Journal of Geology*, *90*(2), 127–138. https://doi.org/10.1086/628658

Bottinga, Y., Weill, D., & Richet, P. (1982). Density calculations for silicate liquids. I. Revised method for aluminosilicate compositions. *Geochimica et Cosmochimica Acta*, *46*(6), 909–919. https://doi.org/10.1016/0016-7037(82)90047-3

Boyd, F. R., England, J. L., & Clark, S. P. (1963). Effect of pressure on the melting of diopside, $CaMgSi_2O_6$, and albite, $NaAlSi_3O_8$, in the range up to 50 kilobars [WITH AN APPENDIX. *Journal of Geophysical Research*, *68*(1), 311–323.

Collinet, M., & Grove, T. L. (2020). Widespread production of silica- and alkali-rich melts at the onset of planetesimal melting. *Geochimica et Cosmochimica Acta*, *277*, 334–357. https://doi.org/10.1016/j.gca.2020.03.005

Crépisson, C., Morard, G., Bureau, H., Prouteau, G., Morizet, Y., Petitgirard, S., & Sanloup, C. (2014). Magmas trapped at the Continental lithosphere–asthenosphere boundary. *Earth and Planetary Science Letters*, *393*, 105–112. https://doi.org/10.1016/j.epsl.2014.02.048

Dziewonski, A. M., & Anderson, D. L. (1981). Preliminary reference Earth model. *Physics of the Earth and Planetary Interiors*, *25*(4), 297–356. https://doi.org/10.1016/0031-9201(81)90046-7

Eaton, D. W., Darbyshire, F., Evans, R. L., Grütter, H., Jones, A. G., & Yuan, X. (2009). The elusive lithosphere–asthenosphere boundary (LAB) beneath cratons. *Lithos*, *109*(1–2), 1–22. https://doi.org/10.1016/j.lithos.2008.05.009

Elardo, S. M., Draper, D. S., & Shearer, C. K. (2011). Lunar magma ocean crystallization revisited: Bulk composition, early cumulate mineralogy, and the source regions of the highlands Mg-suite. *Geochimica et Cosmochimica Acta*, *75*(11), 3024–3045. https://doi.org/10.1016/j.gca.2011.02.033

Elkins-Tanton, L. T., Parmentier, E. M., & Hess, P. C. (2003). Magma ocean fractional crystallization and cumulate overturn in terrestrial planets: Implications for Mars. *Meteoritics & Planetary Sciences*, *38*(12), 1753–1771. https://doi.org/10.1111/j.1945-5100.2003.tb00013.x

Faul, U. H. (2001). Melt retention and segregation beneath mid-ocean ridges. *Nature*, *410*(6831), 920–923. https://doi.org/10.1038/35073556

Fischer, K. M., Ford, H. A., Abt, D. L., & Rychert, C. A. (2010). The lithosphere-asthenosphere boundary. *Annual Review of Earth and Planetary Sciences*, *38*(1), 551–575. https://doi.org/10.1146/annurev-earth-040809-152438

Ford, H. A., Fischer, K. M., Abt, D. L., Rychert, C. A., & Elkins-Tanton, L. T. (2010). The lithosphere–asthenosphere boundary and cratonic lithospheric layering beneath Australia from Sp wave imaging. *Earth and Planetary Science Letters*, *300*(3–4), 299–310. https://doi.org/10.1016/j.epsl.2010.10.007

Foster, K., Dueker, K., Schmandt, B., & Yuan, H. (2014). A sharp cratonic lithosphere–asthenosphere boundary beneath the American midwest and its relation to mantle flow. *Earth and Planetary Science Letters*, *402*(C), 82–89. https://doi.org/10.1016/j.epsl.2013.11.018

Ghiorso, M. S. (2004). An equation of state for silicate melts. IV. Calibration of a multicomponent mixing model to 40 GPa. *American Journal of Science*, *304*(8–9), 811–838. https://doi.org/10.2475/ajs.304.8-9.811

Ghiorso, M. S., & Kress, V. C. (2004). An equation of state for silicate melts. II. Calibration of volumetric properties at 10^5 Pa. *American Journal of Science*, *304*(8–9), 679–751. https://doi.org/10.2475/ajs.304.8-9.679

Ghosh, S., Ohtani, E., Litasov, K., Suzuki, A., & Sakamaki, T. (2007). Stability of carbonated magmas at the base of the Earth's upper mantle. *Geophysical Research Letters*, *34*(22), L22312. https://doi.org/10.1029/2007GL031349

Giordano, D., Russell, J. K., & Dingwell, D. B. (2008). Viscosity of magmatic liquids: A model. *Earth and Planetary Science Letters*, *271*(1–4), 123–134. https://doi.org/10.1016/j.epsl.2008.03.038

Guo, X., Lange, R. A., & Ai, Y. (2013). The density and compressibility of CaO–FeO–SiO_2 liquids at one bar: Evidence for four-coordinated Fe^{2+} in the $CaFeO_2$ component. *Geochimica et Cosmochimica Acta*, *120*, 206–219. https://doi.org/10.1016/j.gca.2013.06.007

Guo, X., Lange, R. A., & Ai, Y. (2014). Density and sound speed measurements on model basalt (An–Di–Hd) liquids at one bar: New constraints on the partial molar volume and compressibility of the FeO component. *Earth and Planetary Science Letters*, *388*, 283–292. https://doi.org/10.1016/j.epsl.2013.12.005

Holness, M. B. (2006). Melt-solid dihedral angles of common minerals in natural rocks. *Journal of Petrology*, *47*(4), 791–800. https://doi.org/10.1093/petrology/egi094

Jing, Z., & Karato, S. (2009). The density of volatile bearing melts in the Earth's deep mantle: The role of chemical composition. *Chemical Geology*, *262*(1–2), 100–107. https://doi.org/10.1016/j.chemgeo.2009.02.019

Jing, Z., & Karato, S. (2011). A new approach to the equation of state of silicate melts: An application of the theory of hard sphere mixtures. *Geochimica et Cosmochimica Acta*, *75*(22), 6780–6802. https://doi.org/10.1016/j.gca.2011.09.004

Jing, Z., & Karato, S. (2012). Effect of H_2O on the density of silicate melts at high pressures: Static experiments and the application of a modified hard-sphere model of equation of state. *Geochimica et Cosmochimica Acta*, *85*, 357–372. https://doi.org/10.1016/j.gca.2012.03.001

Jing, Z., & Karato, S. i. (2008). Compositional effect on the pressure derivatives of bulk modulus of silicate melts. *Earth and Planetary Science Letters*, *272*(1–2), 429–436. https://doi.org/10.1016/j.epsl.2008.05.013

Jones, A. G. (1999). Imaging the Continental upper mantle using electromagnetic methods. *Lithos*, *48*(1–4), 57–80. https://doi.org/10.1016/S0024-4937(99)00022-5

Karlsson, C., Zanghellini, E., Swenson, J., Roling, B., Bowron, D. T., & Börjesson, L. (2005). Structure of mixed alkali/alkaline-earth silicate glasses from neutron diffraction and vibrational spectroscopy. *Physical Review B*, *72*(6), 064206. https://doi.org/10.1103/PhysRevB.72.064206

Katsura, T. (2022). A revised adiabatic temperature profile for the mantle. *Journal of Geophysical Research: Solid Earth*, *127*(2), 1–11. https://doi.org/10.1029/2021JB023562

Kennett, B. L. N., & Engdahl, E. R. (1991). Traveltimes for global earthquake location and phase identification. *Geophysical Journal International*, *105*(2), 429–465. https://doi.org/10.1111/j.1365-246X.1991.tb06724.x

Ketcham, R. A. (2005). Computational methods for quantitative analysis of three-dimensional features in geological specimens. *Geosphere*, *1*(1), 32–41. https://doi.org/10.1130/GES00001.1

Ketcham, R. A., & Carlson, W. D. (2001). Acquisition, optimization and interpretation of X-ray computed tomographic imagery: Applications to the geosciences. *Computers and Geosciences*, *27*(4), 381–400. https://doi.org/10.1016/S0098-3004(00)00116-3

Knoche, R., & Luth, R. W. (1996). Density measurements on melts at high pressure using the sink/float method: Limitations and possibilities. *Chemical Geology*, *128*(1–4), 229–243. https://doi.org/10.1016/0009-2541(95)00176-X

Kress, V. C., & Carmichael, I. S. E. (1991). The compressibility of silicate liquids containing Fe_2O_3 and the effect of composition, temperature, oxygen fugacity and pressure on their redox states. *Contributions to Mineralogy and Petrology*, *108*(1–2), 82–92. https://doi.org/10.1007/BF00307328

Kress, V. C., Williams, Q., & Carmichael, I. S. E. (1988). Ultrasonic investigation of melts in the system Na_2O-Al_2O_3-SiO_2. *Geochimica et Cosmochimica Acta*, *52*(2), 283–293. https://doi.org/10.1016/0016-7037(88)90084-1

Lange, R. A. (1994). The effect of H_2O, CO_2 and F on the density and viscosity of silicate melts. In M. R. Carroll & J. R. Holloway (Eds.), *Volatiles in magmas* (pp. 331–369). Mineralogical Society of America.

Lange, R. A. (1997). A revised model for the density and thermal expansivity of K_2O-Na_2O-CaO-MgO-Al_2O_3-SiO_2 liquids from 700 to 1900 K: Extension to crustal magmatic temperatures. *Contributions to Mineralogy and Petrology*, *130*(1), 1–11. https://doi.org/10.1007/s004100050345

Lange, R. A., & Carmichael, I. S. E. (1987). Densities of Na_2O-K_2O-CaO-MgO-FeO-Fe_2O_3-Al_2O_3-TiO_2-SiO_2 liquids: New measurements and derivated partial molar properties. *Geochimica et Cosmochimica Acta*, *51*(11), 2931–2946. https://doi.org/10.1016/0016-7037(87)90368-1

Lange, R. A., & Navrotsky, A. (1992). Heat capacities of Fe_2O_3-bearing silicate liquids. *Contributions to Mineralogy and Petrology*, *110*(2–3), 311–320. https://doi.org/10.1007/BF00310746

Lebowitz, J. L. (1964). Exact solution of generalized percus-yevick equation for a mixture of hard spheres. *Physical Review*, *133*(4A), A895–A899. https://doi.org/10.1103/PhysRev.133.A895

Lebowitz, J. L., Helfand, E., & Praestgaard, E. (1965). Scaled particle theory of fluid mixtures. *The Journal of Chemical Physics*, *43*(3), 774–779. https://doi.org/10.1063/1.1696842

Lesher, C. E., Wang, Y., Gaudio, S., Clark, A., Nishiyama, N., & Rivers, M. (2009). Volumetric properties of magnesium silicate glasses and supercooled liquid at high pressure by X-ray microtomography. *Physics of the Earth and Planetary Interiors*, *174*(1–4), 292–301. https://doi.org/10.1016/j.pepi.2008.10.023

Lichtenberg, T., Keller, T., Katz, R. F., Golabek, G. J., & Gerya, T. V. (2019). Magma ascent in planetesimals: Control by grain size. *Earth and Planetary Science Letters*, *507*, 154–165. https://doi.org/10.1016/j.epsl.2018.11.034

Litvin, Y. A., & Gasparik, T. (1993). Melting of jadeite to 16.5 GPa and melting relations on the enstatite-jadeite join. *Geochimica et Cosmochimica Acta*, *57*(9), 2033–2040. https://doi.org/10.1016/0016-7037(93)90091-A

Lunning, N. G., Gardner-Vandy, K. G., Sosa, E. S., McCoy, T. J., Bullock, E. S., & Corrigan, C. M. (2017). Partial melting of oxidized planetesimals: An experimental study to test the formation of oligoclase-rich achondrites graves nunataks 06128 and 06129. *Geochimica et Cosmochimica Acta*, *214*, 73–85. https://doi.org/10.1016/j.gca.2017.07.004

Malfait, W. J., Seifert, R., Petitgirard, S., Mezouar, M., & Sanchez-Valle, C. (2014b). The density of andesitic melts and the compressibility of dissolved water in silicate melts at crustal and upper mantle conditions. *Earth and Planetary Science Letters*, *393*, 31–38. https://doi.org/10.1016/j.epsl.2014.02.042

Malfait, W. J., Seifert, R., Petitgirard, S., Perrillat, J.-P., Mezouar, M., Ota, T., et al. (2014a). Supervolcano eruptions driven by melt buoyancy in large silicic magma chambers. *Nature Geoscience*, *7*(12), 122–125. https://doi.org/10.1038/ngeo2042

Matsukage, K. N., Jing, Z., & Karato, S. (2005). Density of hydrous silicate melt at the conditions of Earth's deep upper mantle. *Nature*, *438*(7067), 488–491. https://doi.org/10.1038/nature04241

McKenzie, D. (1985). The extraction of magma from the crust and mantle. *Earth and Planetary Science Letters*, *74*(1), 81–91. https://doi.org/10.1016/0012-821X(85)90168-2

Monnereau, M., Guignard, J., Néri, A., Toplis, M. J., & Quitté, G. (2023). Differentiation time scales of small rocky bodies. *Icarus*, *390*, 115294. https://doi.org/10.1016/j.icarus.2022.115294

Moskovitz, N., & Gaidos, E. (2011). Differentiation of planetesimals and the thermal consequences of melt migration. *Meteoritics & Planetary Sciences*, *46*(6), 903–918. https://doi.org/10.1111/j.1945-5100.2011.01201.x

Mysen, B. O., Virgo, D., & Scarfe, C. M. (1980). Relations between the anionic structure and viscosity of silicate melts-a Raman spectroscopic study. *American Mineralogist*, *65*, 690–710.

Nakagawa, T., & Tackley, P. J. (2012). Influence of magmatism on mantle cooling, surface heat flow and Urey ratio. *Earth and Planetary Science Letters*, *329–330*, 1–10. https://doi.org/10.1016/j.epsl.2012.02.011

Navrotsky, A., Geisinger, K. L., McMillan, P., & Gibbs, G. V. (1985). The tetrahedral framework in glasses and melts? Inferences from molecular orbital calculations and implications for structure, thermodynamics, and physical properties. *Physics and Chemistry of Minerals*, *11*(6), 284–298. https://doi.org/10.1007/BF00307406

Nicklas, R. W., Day, J. M. D., Gardner-Vandy, K. G., & Udry, A. (2022). Early silicic magmatism on a differentiated asteroid. *Nature Geoscience*, *15*(9), 696–699. https://doi.org/10.1038/s41561-022-00996-1

Ohtani, E., & Maeda, M. (2001). Density of basaltic melt at high pressure and stability of the melt at the base of the lower mantle. *Earth and Planetary Science Letters*, *193*(1–2), 69–75. https://doi.org/10.1016/S0012-821X(01)00505-2

Okuno, M., & Marumo, F. (1982). The structures of anorthite and albite melts. *Mineralogical Journal*, *11*(4), 180–196. https://doi.org/10.2465/minerj.11.180

Pichavant, M., Di Carlo, I., Le Gac, Y., Rotolo, S. G., & Scaillet, B. (2009). Experimental constraints on the deep magma feeding system at Stromboli volcano, Italy. *Journal of Petrology*, *50*(4), 601–624. https://doi.org/10.1093/petrology/egp014

Pohl, L., & Britt, D. T. (2020). Strengths of meteorites—An overview and analysis of available data. *Meteoritics & Planetary Sciences*, *55*(4), 962–987. https://doi.org/10.1111/maps.13449

Poudjom Djomani, Y. H., O'Reilly, S. Y., Griffin, W. L., & Morgan, P. (2001). The density structure of subcontinental lithosphere through time. *Earth and Planetary Science Letters*, *184*(3–4), 605–621. https://doi.org/10.1016/S0012-821X(00)00362-9

Rivers, M. L. (2016). Synchrotron "pink beam" tomography for the study of dynamic processes. In *Spie*. https://doi.org/10.1117/2.1201608.006674

Rivers, M. L., & Carmichael, I. S. E. (1987). Ultrasonic studies of silicate melts. *Journal of Geophysical Research*, *92*(B9), 9247–9270. https://doi.org/10.1029/jb092ib09p09247

Rivers, M. L., & Wang, Y. (2006). Recent developments in microtomography at GeoSoilEnviroCARS. In *Proceedings of SPIE*, 63180J–1. https://doi.org/10.1117/12.681144

Rogers, N. (2015). The composition and origin of magmas. In *The encyclopedia of volcanoes* (2nd ed., pp. 93–112). Elsevier. https://doi.org/10.1016/B978-0-12-385938-9.00004-3

Rychert, C. A., Fischer, K. M., & Rondenay, S. (2005). A sharp lithosphere–asthenosphere boundary imaged beneath eastern North America. *Nature*, *436*(7050), 542–545. https://doi.org/10.1038/nature03904

Sakamaki, T. (2017). Density of jadeite melts under high pressure and high temperature conditions. *Journal of Mineralogical and Petrological Sciences*, *112*(5), 300–307. https://doi.org/10.2465/jmps.170128

Sakamaki, T., Kono, Y., Wang, Y., Park, C., Yu, T., Jing, Z., & Shen, G. (2014). Contrasting sound velocity and intermediate-range structural order between polymerized and depolymerized silicate glasses under pressure. *Earth and Planetary Science Letters*, *391*, 288–295. https://doi.org/10.1016/j.epsl.2014.02.008

Sakamaki, T., Ohtani, E., Urakawa, S., Suzuki, A., & Katayama, Y. (2010). Density of dry peridotite magma at high pressure using an X-ray absorption method. *American Mineralogist*, *95*(1), 144–147. https://doi.org/10.2138/am.2010.3143

Sakamaki, T., Suzuki, A., Ohtani, E., Terasaki, H., Urakawa, S., Katayama, Y., & Ballmer, M. D. (2013). Ponded melt at the boundary between the lithosphere and asthenosphere TL - 6. *Nature Geoscience, 6 VN-re(October)*, 10411044. https://doi.org/10.1038/ngeo1982

Sanloup, C. (2016). Density of magmas at depth. *Chemical Geology*, *429*, 51–59. https://doi.org/10.1016/j.chemgeo.2016.03.002

Sanloup, C., Drewitt, J. W. E., Konôpková, Z., Dalladay-Simpson, P., Morton, D. M., Rai, N., et al. (2013). Structural change in molten basalt at deep mantle conditions. *Nature*, *503*(7474), 104–107. https://doi.org/10.1038/nature12668

Secco, R. A., Manghnani, M. H., & Liu, T.-C. (1991). The bulk modulus - attenuation - viscosity systematics of diopside-anorthite melts. *Geophysical Research Letters*, *18*(1), 93–96. https://doi.org/10.1029/90GL01711

Seifert, R., Malfait, W. J., Petitgirard, S., & Sanchez-Valle, C. (2013). Density of phonolitic magmas and time scales of crystal fractionation in magma chambers. *Earth and Planetary Science Letters*, *381*, 12–20. https://doi.org/10.1016/j.epsl.2013.08.039

Shankland, T. J., O'Connell, R. J., & Waff, H. S. (1981). Geophysical constraints on partial melt in the upper mantle. *Reviews of Geophysics and Space Physics*, *19*(3), 394–406.

Sisson, T. W., & Bacon, C. R. (1999). Gas-driven filter pressing in magmas. *Geology*, *27*(7), 613. https://doi.org/10.1130/0091-7613(1999)027<0613:GDFPIM>2.3.CO;2

Sleep, N. H. (1988). Tapping of melt by veins and dikes. *Journal of Geophysical Research*, *93*(B9), 10255–10272. https://doi.org/10.1029/JB093iB09p10255

Solferino, G. F. D., Thomson, P.-R., & Hier-Majumder, S. (2020). Pore network modeling of core forming melts in planetesimals. *Frontiers in Earth Science*, *8*(August), 1–15. https://doi.org/10.3389/feart.2020.00339

Stolper, E., Walker, D., Hager, B. H., & Hays, J. F. (1981). Melt segregation from partially molten source regions: The importance of melt density and source region size. *Journal of Geophysical Research*, *86*(B7), 6261–6271. https://doi.org/10.1029/jb086ib07p06261

Suzuki, A., & Ohtani, E. (2003). Density of peridotite melts at high pressure. *Physics and Chemistry of Minerals*, *30*(8), 449–456. https://doi.org/10.1007/s00269-003-0322-6

Suzuki, A., Ohtani, E., & Kato, T. (1998). Density and thermal expansion of a peridotite melt at high pressure. *Physics of the Earth and Planetary Interiors*, *107*(1–3), 53–61. https://doi.org/10.1016/S0031-9201(97)00123-4

Takazawa, E., Sekine, T., Kobayashi, T., & Zhu, Y. (1998). Hugoniot equation of state and high-pressure transformation of jadeite. *Journal of Geophysical Research*, *103*(B6), 12261–12268. https://doi.org/10.1029/98jb00767

Tange, Y., Nishihara, Y., & Tsuchiya, T. (2009). Unified analyses for *P* - *V* - *T* equation of state of MgO: A solution for pressure-scale problems in high *P* - *T* experiments. *Journal of Geophysical Research*, *114*(B3), B03208. https://doi.org/10.1029/2008JB005813

Tenner, T. J., Lange, R. A., & Downs, R. T. (2007). The albite fusion curve re-examined: New experiments and the high-pressure density and compressibility of high albite and NaAlSi3O8 liquid. *American Mineralogist*, *92*(10), 1573–1585. https://doi.org/10.2138/am.2007.2464

Thomas, C. W., & Asimow, P. D. (2013). Preheated shock experiments in the molten $CaAl_2Si_2O_8$-$CaFeSi_2O_6$-$CaMgSi_2O_6$ ternary: A test for linear mixing of liquid volumes at high pressure and temperature. *Journal of Geophysical Research: Solid Earth*, *118*(7), 3354–3365. https://doi.org/10.1002/jgrb.50269

Ueki, K., & Iwamori, H. (2016). Density and seismic velocity of hydrous melts under crustal and upper mantle conditions. *Geochemistry, Geophysics, Geosystems*, *17*(5), 1799–1814. https://doi.org/10.1002/2015GC006242

Usui, T., Jones, J. H., & Mittlefehldt, D. W. (2015). A partial melting study of an ordinary (H) chondrite composition with application to the unique achondrite graves Nunataks 06128 and 06129. *Meteoritics & Planetary Sciences*, *50*(4), 759–781. https://doi.org/10.1111/maps.12392

Wang, Y., Sakamaki, T., Skinner, L. B., Jing, Z., Yu, T., Kono, Y., et al. (2014). Atomistic insight into viscosity and density of silicate melts under pressure. *Nature Communications*, *5*, 1–10. https://doi.org/10.1038/ncomms4241

Wang, Y., Uchida, T., Westferro, F., Rivers, M. L., Nishiyama, N., Gebhardt, J., et al. (2005). High-pressure x-ray tomography microscope: Synchrotron computed microtomography at high pressure and temperature. *Review of Scientific Instruments*, *76*(7), 073709. https://doi.org/10.1063/1.1979477

Webb, S., & Courtial, P. (1996). Compressibility of melts in the CaO-Al_2O_3-SiO_2 system. *Geochimica et Cosmochimica Acta*, *60*(1), 75–86. https://doi.org/10.1016/0016-7037(95)00381-9

Xu, M., Jing, Z., Bajgain, S. K., Mookherjee, M., Van Orman, J. A., Yu, T., & Wang, Y. (2020b). High-pressure elastic properties of dolomite melt supporting carbonate-induced melting in deep upper mantle. *Proceedings of the National Academy of Sciences*, *117*(31), 18285–18291. https://doi.org/10.1073/pnas.2004347117

Xu, M., Jing, Z., Chantel, J., Jiang, P., Yu, T., & Wang, Y. (2018). Ultrasonic velocity of diopside liquid at high pressure and temperature: Constraints on velocity reduction in the upper mantle due to partial melts. *Journal of Geophysical Research: Solid Earth*, *123*(10), 8676–8690. https://doi.org/10.1029/2018JB016187

Xu, M., Jing, Z., Van Orman, J. A., Hu, Q., Chen, Q., Yu, T., & Wang, Y. (2025). Data for "Density of sodium aluminosilicate melts along the NaAlSiO4-NaAlSi3O8 join at high pressure: In-situ measurements and re-calibration of a modified hard-sphere equation of state for silicate melts." [Dataset]. *Mendeley Data*. https://doi.org/10.17632/gr892kdjt5.1

Xu, M., Jing, Z., Van Orman, J. A., Yu, T., & Wang, Y. (2020a). Density of $NaAlSi_2O_6$ melt at high pressure and temperature measured by In-Situ X-ray Microtomography. *Minerals*, *10*(2), 161. https://doi.org/10.3390/min10020161

Yoshino, T., Yamazaki, D., & Mibe, K. (2009). Well-wetted olivine grain boundaries in partially molten peridotite in the asthenosphere. *Earth and Planetary Science Letters*, *283*(1–4), 167–173. https://doi.org/10.1016/j.epsl.2009.04.007

Yu, T., Wang, Y., & Rivers, M. L. (2016). Imaging in 3D under pressure: A decade of high-pressure X-ray microtomography development at GSECARS. *Progress in Earth and Planetary Science*, *3*(17), 17. https://doi.org/10.1186/s40645-016-0093-6

Yuan, H., & Romanowicz, B. (2010). Lithospheric layering in the North American craton. *Nature*, *466*(7310), 1063–1068. https://doi.org/10.1038/nature09332

Zhang, Z., Bercovici, D., & Elkins-Tanton, L. T. (2023). Melt migration in rubble-pile planetesimals: Implications for the formation of primitive achondrites. *Earth and Planetary Science Letters*, *605*, 118019. https://doi.org/10.1016/j.epsl.2023.118019

Zhao, C., Garnero, E. J., McNamara, A. K., Schmerr, N., & Carlson, R. W. (2015). Seismic evidence for a chemically distinct thermochemical reservoir in Earth's deep mantle beneath Hawaii. *Earth and Planetary Science Letters*, *426*, 143–153. https://doi.org/10.1016/j.epsl.2015.06.012

Zhou, W.-Y., Hao, M., Hrubiak, R., Kenney-Benson, C., & Zhang, J. S. (2024). Migration and accumulation of hydrous mantle incipient melt in the Earth's asthenosphere: Constraints from in-situ falling sphere viscometry measurements. *Earth and Planetary Science Letters*, *641*(February), 118833. https://doi.org/10.1016/j.epsl.2024.118833